MULTI-OBJECTIVE OPTIMIZATION OF A CENTRIFUGAL FAN BASED ON FLOW SIMULATIONS

By

Onur YENİGÜL

Submitted to the Institute of Graduate Studies in

Science and Engineering in partial fulfillment of

the requirements for the degree of

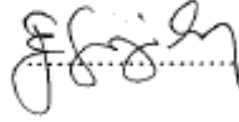Master of Science

in

Mechanical Engineering

Yeditepe University

2010

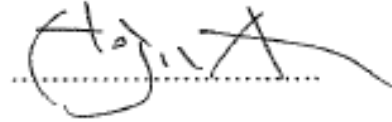# MULTI-OBJECTIVE OPTIMIZATION OF A CENTRIFUGAL FAN BASED ON FLOW SIMULATIONS

APPROVED BY:

Asst. Prof. Esra Sorgüven   ....
(Thesis Supervisor)

Assoc. Prof. Hojin Ahn   ....

Asst. Prof. Levent Kavurmacıoğlu   ....

DATE OF APPROVAL: / /2010

ACKNOWLEDGEMENT

ABSTRACT

MULTI-OBJECTIVE OPTIMIZATION OF A CENTRIFUGAL FAN BASED ON FLOW SIMULATIONS

As a type of turbomachinery, centrifugal fans are widely used for gaseous transportation in industrial applications due to their large capacity of mass flow and compactness. During the operation time fans make noise. Because of the strict environmental noise restrictions and recent market demands, noise reduction is one of the challenges that suppliers have to face. The manufacturers are focused on providing adequate performance while keeping the noise level as low as possible. Many machines having low efficiency and low aeroacoustic performances are still in operation and could be improved by using today's technological facilities. Therefore, the noise generated by fans is receiving an increasing research interest in recent years. Most prior noise analysis study has dealt with theoretical formulations or experimental measurements on noise generation. Many reviewed researches based on numerical analysis are available in literature but very little work has been done so far on aerodynamic and aeroacoustic optimization of centrifugal fans. The aim of this project is to develop a multi-objective optimization methodology by making use of flow simulations.

ÖZET

MULTI-OBJECTIVE OPTIMIZATION OF A CENTRIFUGAL FAN BASED ON FLOW SIMULATIONS

Turbomakinaların bir türü olan radyal fanlar endüstriyel uygulamalarda yüksek debi kapasiteleri ve kompakt yapıları nedeniyle gaz taşınması için yaygın olarak kullanılmaktadır. Fanlar çalışırken gürültüye neden olurlar. Çevresel gürültü kısıtlamaları ve güncel pazar talepleri nedeniyle, gürültü azaltma üreticilerin yüzleşmek zorunda olduğu bir durumdur. Üreticiler gerekli performansı sağlarken en düşük gürültü seviyesini sağlamaya odaklanmışlardır. Halen kullanılmakta olan düşük verimliliğe ve aeroakustik performansa sahip makinalar günümüz teknolojik olanakları kullanılarak geliştirilebilir. Bu nedenle, fan kaynaklı gürültü konusu son yıllarda artan araştırma ilgisi görmektedir. Daha önce yapılan gürültü analiz çalışmaları teorik formülasyonlar veya deneysel gürültü ölçümlerini kapsamaktadır. Sayısal analiz içerikli birçok araştırmada literatürde yer almaktadır fakat şimdiye kadar aerodinamik ve aeroakustik radyal fan optimizasyonu üzerine yapılmış olan çok az sayıda çalışma bulunmaktadır. Bu projenin amacı akış simülasyonlarını kullanarak radyal fanlar için çok amaçlı optimizasyon yöntemi geliştirmektir.

TABLE OF CONTENTS

LIST OF FIGURES

LIST OF TABLES

LIST OF SYMBOLS / ABBREVIATIONS

c	Speed of Sound
c_0	Number of Center Points
I_{ref}	Reference Sound Intensity
k	Turbulent Kinetic Energy
l_c	Turbulent Length Scale
L_w	Sound Power Level
P_{ref}	Threshold of Hearing
Pr_t	Turbulent Prandtl Number
pr_{tt}	Total-to-Total Pressure Ratio
W_{ref}	Reference Sound Power
ε	Turbulent Dissipation
η_{tt}	Total-to-Total Efficiency
η_u	Hydraulic Efficiency
μ_T	Turbulent Viscosity
ρ	Density
τ_{ij}	Viscous Stress Tensor
υ	Kinematic Viscosity
ω	Specific Dissipation
ANN	Artificial Neural Network
BPF	Blade Passing Frequency
BBD	Box-Behnken Design
CCD	Central Composite Design
CFD	Computational Fluid Dynamics
DNS	Direct Numerical Simulation
DOE	Design of Experiment
FFT	Fast Fourier Transform
FVM	Finite Volume Method

FW-H	Ffowcs Williams and Hawkings
GA	Genetic Algorithm
LES	Large Eddy Simulation
PIV	Particle Image Velocimetry
RANS	Reynolds-Averaged Navier Stokes
RNG	Re-Normalization Group
RSM	Response Surface Methodology
SIL	Sound Intensity Level
SPL	Sound Pressure Level

1. INTRODUCTION

Turbomachinery is widely used for exchanging mechanical energy and fluid energy continuously. It can be classified into several categories such as fans, compressors, turbines, pumps etc. according to the types of working fluid and directions of energy exchange. Fans can generate pressure rises in the gas stream. There are three main types of fans used for moving gases: axial, centrifugal and crossflow. In a centrifugal fan, a gas is radially accelerated outward in an impeller to a surrounding casing. Centrifugal fans are often used in mechanical systems because they can provide higher pressure rise than other types of similar-sized turbomachinery.

There is an increasing market demand for consumer products with low noise emission and energy consumption. To reduce energy consumption, the aerodynamic performance of turbomachinery used in consumer products must be improved as much as possible. With the significant improvements in computer technology, numerical optimization methods became available. The single-objective optimization methods have been frequently applied in turbomachinery designs in order to improve the aerodynamic performance. The single-objective optimization approach is useful when multiple design objectives are reduced into a single objective with reasonable assumptions. However, in general, minimizing noise and maximizing aerodynamic performance are conflicting objectives. Fans with higher efficiency are usually noisier. For this reason, multiple design objectives need to be optimized simultaneously.

Most of the previous studies focused on axial turbomachinery configurations. In contrast, fewer works were found for centrifugal ones. Therefore, centrifugal configurations are the main focus of interest in this study. Previous studies about design optimization of centrifugal turbomachinery are summarized in Chapter 2. The majority of them were only focused on improving the aerodynamic performance. Only few of them involve multi-objective optimization application.

The theoretical background information of response surface based on design optimization features and noise measurement characteristics are described in Chapter 3.

The detailed explanation about computational fluid dynamics and design of experiment method is given.

Chapter 4 explains two-dimensional-simulation-based multi-objective optimization method. This method was applied to the design of centrifugal pump for a washing machine. Based on transient CFD results, optimal design of centrifugal pump was proposed.

The application of three-dimensional multi-objective optimization approach for designing a centrifugal fan that is aerodynamically and aeroacoustically efficient is reported in Chapter 5. Numerical results were experimentally validated. The prototypes of new designs were produced and used in the experiments. The acoustic behaviour of baseline and optimal configurations was characterized by means of sound power level measurements. The noise measurements were conducted in a semi-anechoic test room. The capability of optimization method was demonstrated by comparing the test results.

Chapter 6 presents final conclusions of this optimization study and comments on effectiveness of the proposed multi-objective method for centrifugal turbomachinery configuration designs.

The tables of DOE matrix including all sets of combinations, numerically predicted responses and correlation matrix representing the influence of design variables on responses are given in Appendix A.

2. LITERATURE SURVEY

In the literature, the majority of prior studies have focused on aerodynamic shape optimization of turbomachinery blades and cut-off in a fan-volute system. A few researches on aeroacoustic optimization of turbomachinery have been reported.

Grapsas et al. [1] have studied on the maximization of pump impeller's efficiency by adjusting the blade length and the number of blades. The method is based on the combination of a numerical code and an optimization algorithm. Numerical code is capable of creating two-dimensional blade and geometry and calculating the flow field.

The blade length was adjusted by wrap angle θ_w. In order to find wrap angle that maximizes hydraulic efficiency (η_u), optimization software of EASY was used. By applying the optimization algorithm for the impellers with wrap angle θ_w= 54.1, 58.5, 68.6, 77.8, 98.1, 122.6, the optimal wrap angle was determined as 72.62°. Figure 2.1 illustrates the comparison of the optimized blade and the initial blade. It was observed that the performance of the optimized impeller is approximately 2.5% higher in comparison to initial blade shape when pump operates with a volume flow rate of 62.5 m^3/h.
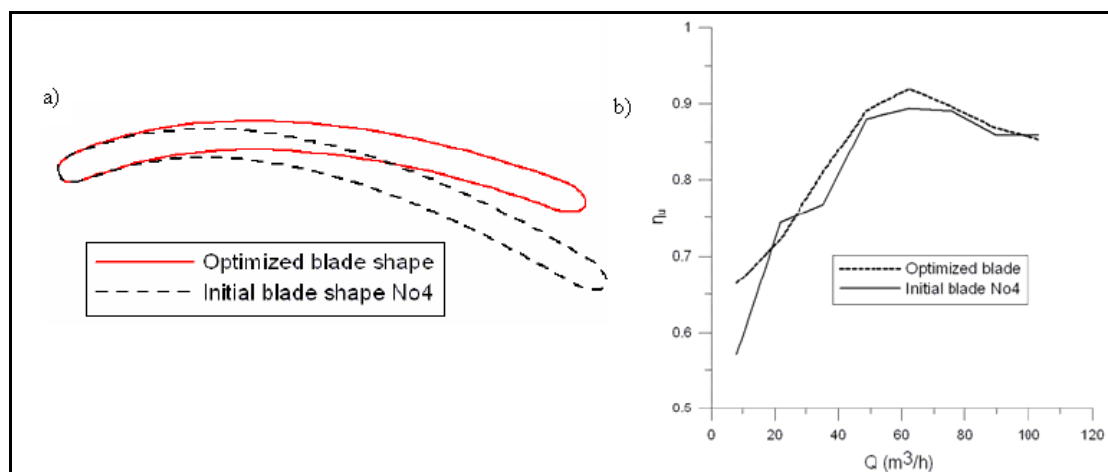
Figure 2.1. Comparison of a. blade shapes and b. hydraulic efficiencies

The optimization study for the blade length was repeated for a different number of blades ranging from 6 to 11. More blades guide the flow better but lead to thinner passages between blades, causing blockage effect. From the optimization procedure it was found that the impeller with 9 blades presents the maximum efficiency as shown in Figure 2.2. In addition, it was noted that the optimum blade length decreases as the number of blades increases.
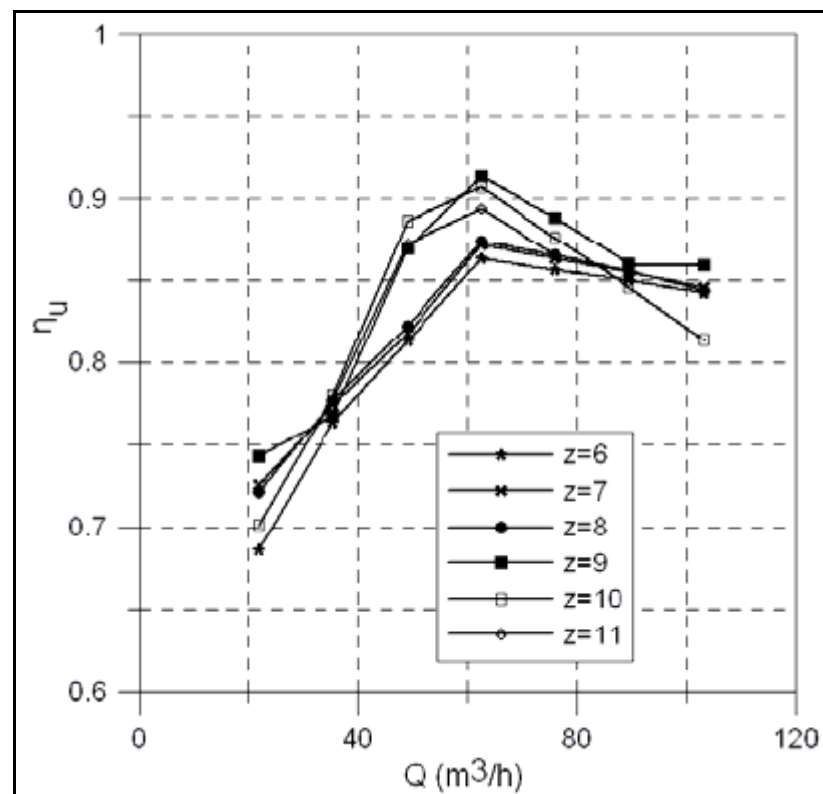
Figure 2.2. Variation of characteristic curves for different number of blades [1]

In the work of Burguburu et al. [2], the 3D Navier-Stokes solver was coupled to a gradient-based method to optimize a transonic compressor. The optimization was carried out by modifying the suction surface of the blade with a deformation function defined by a Bezier curve.

The optimization methodology is composed of four main parts. The optimization tool supplies design variable and then the grid deformation tool generates a new mesh. The aerodynamic field is updated by a steady Navier-Stokes code and finally the objective

function and constraints are deduced from the flow results that are computed by averaging total mass flow, pressure ratio, temperature ratio and efficiency.

The deformation surface is defined by Bezier surface which has 7 control points in the ξ direction and 4 control points in η direction (Fig. 2.3). The Bezier surface is defined by relation:

$$\vec{R} = \sum_{k=0}^{n} \left\{ \sum_{l=0}^{m} P_{k,l} B_{l}^{m}(v) \right\} B_{k}^{n}(u) \qquad (2.1)$$

where B_{k}^{n} is the Bernstein polynomial.
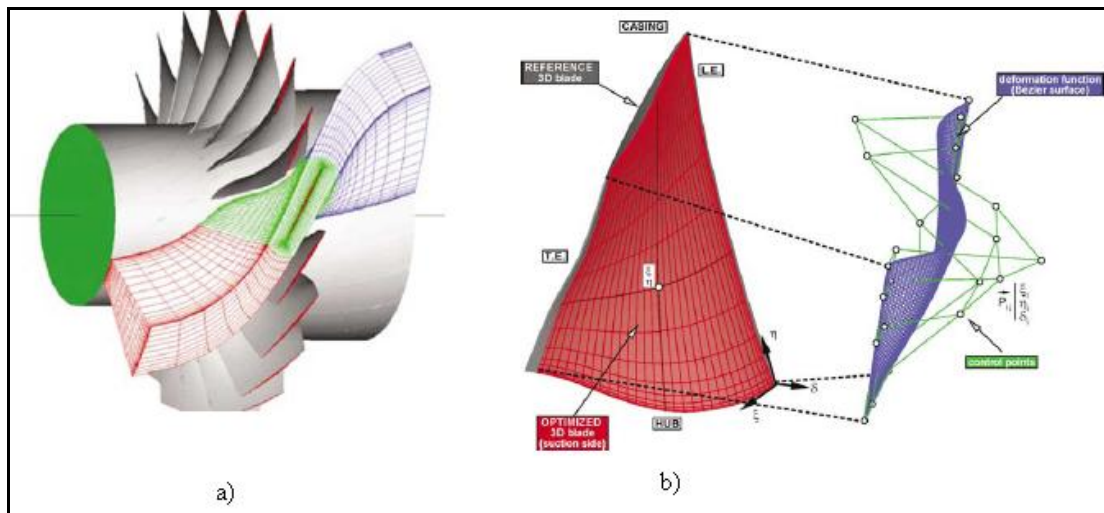
Figure 2.3. a. Computational grid view b. Blade deformation function [2]

It was concluded that the optimized blade improves the efficiency. The losses are largely diminished by reducing rotor wake thickness and the tip clearance effects.

Since aerodynamic design optimization problems are complex with possibly many local minima, gradient based methods have a risk of getting trapped in a local optimum. For this reason, genetic algorithm (GA) is adopted by many researchers to ensure reaching close to the global minimum.

GAs are general purpose algorithms inspired by evolution observed in nature. Genetic algorithms start with randomly generated candidate solutions. Then, high quality parents are selected and their genetic representations are recombined to produce offspring solutions. Offsprings are subjected to a small amount of mutation. This process continues until a satisfactory solution is obtained. One drawback of GA is that the required CPU time is usually not practical. The examples of GAs applied in turbomachinery design problems are given by Mengistu et al. [3], Pierret [4] and Kelner et al. [5].

Pierret preferred GA methodology that accelerates optimization process of three dimensional turbomachinery blades by using approximate model and efficient genetic operators. The NASA rotor 67 geometry was optimized for a large number of design variables to demonstrate the capabilities of the method. The blade design methodology is organized with the following five steps [4]:

1. The first step consists of building a database using a design of experiment procedure.

2. Then an approximate model is built using the DOE points in order to construct an analytical relation between the design variables and the simulation responses.

3. Third, an optimization algorithm is used to find the optimum using the approximate model to evaluate the objective functions and constraints.

4. Then the accurate simulation is used to evaluate and verify the real objective function and constraint values. This new simulation result is added to the database. The database is therefore always improved with new design points, thus leading to improved approximate model.

5. Go to step 2 until the maximum number of optimization specified by the user is not reached.

The optimal geometry was found for three different operating conditions. The same optimization problem has been solved with both the combination of GA and approximate model, and simple GA alone. It was concluded that the use of approximate model together with the genetic algorithm is at least 20 times faster than a simple genetic algorithm.

Neural networks are other well-known mathematical optimization methods. They imitate the way in which the brain works. Neural networks consist of fully interconnected layers called neurons. There is always one input and one output layer, and at least one hidden layer. Each layer of nodes receives its input from the previous layer. The optimization process is nonlinear and consists of iteratively varying the model information containing connections between neurons in successive layers.

Han et al. [6] investigated optimal angle and radius of cut-off using two-dimensional CFD and neural network. The ranges of the angle and radius were determined as 67°-77° and $0.06D_2$ and $0.12D_2$, respectively. A neural network (Fig.2.1) was constructed using Matlab. Volume flow rates that are an only response were obtained from CFD analysis for each combination and used as target values in neural network. The optimal angle and radius were determined as 71° and $0.092D_2$.
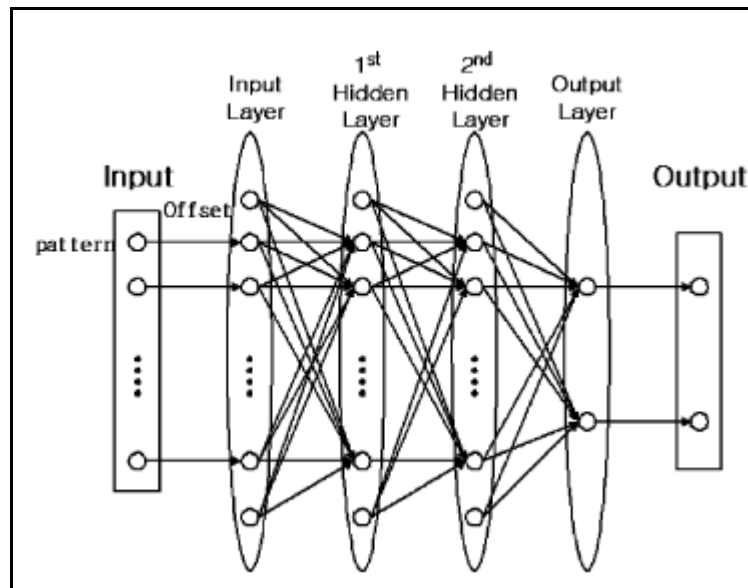
Figure 2.4. Structure of neural network [6]

In a study by Mengistu and Ghaly [3], GA was combined with an artificial neural network (ANN) that uses a back propagation algorithm. The developed simulation based optimization scheme was applied to multi-point optimization of a NACA 65 subsonic compressor rotor in two-dimensional flow. The blade profile was modeled using non-uniform rational B-splines (NURBS) with control points. The positions of these control

points were taken as the design parameters. The ANN model was constructed with output layer containing four output variables: efficiency reduced mass flow rate, inlet flow angle and exit flow angle.

The aerodynamic design optimization consists of four basic steps: blade geometry parameterization using NURBS, numerical optimization using GA, response surface approximation using multi-layer network for the low fidelity calculation of the objective functions and constraints and flow simulation for the high fidelity calculation. The detailed schematic view of optimization process is illustrated in Figure 2.3.

The use of ANN model to approximate the optimization objective and constraints was found to reduce the computing time by a factor of ten. The resultant optimal blade design showed improvement of 7% in efficiency and 1% in total pressure ratio. It was concluded that the developed methodology is capable of improving the blade performance over the full operating range by reshaping the blade profile and simultaneously satisfying the design constraints.
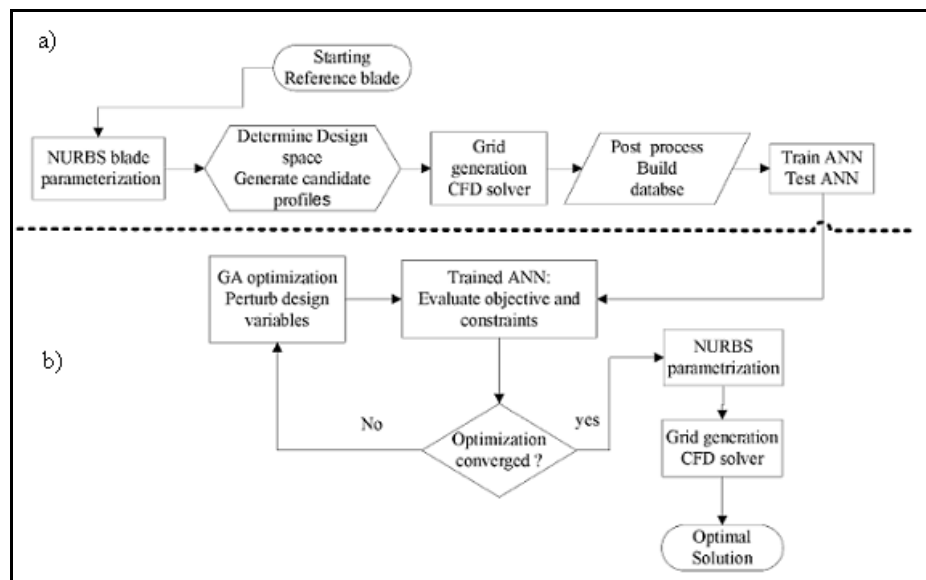
Figure 2.5. The ANN based process a. Construction of ANN model b. Optimization

By Sun, Shin and Lee [7], the optimization procedure including response surface method and genetic algorithm is combined with Navier-Stokes solver for flow simulation

and FW-H equation for the noise prediction was developed. The aim was to obtain advanced impeller geometry for centrifugal compressor with high aerodynamic performance and low noise characteristics.

The effect of six geometrical parameters having a dominant effect on the performance and noise generation were analyzed. The sound pressure level (SPL) calculations at the first blade passing frequency from the impeller inlet and outlet was performed at 1 m away from the impeller center using the computed pressure data of numerical simulations. The objective function and the constraint of multi objective optimization were selected as follows:

Objective: minimize $we_1 / \eta_{tt} + we_2 \times SPL_{in} + we_3 \times SPL_{out}$

Constraint: $pr_{tt} \geq (pr_{tt})_{baseline}$

where we_1, we_2, we_3 are the weighting factors, pr_{tt} and η_{tt} are total-to-total pressure ratio and efficiency, respectively. The weighting factors are selected to be 0.3333.

The numerical simulations show a good agreement with response surface model results except SPL at the impeller inlet. This result was related to fitting quality of the response surface model. Table 2.1 shows the comparison of numerically calculated responses of aerodynamic and aeroacoustic performance in baseline and optimized impeller blades. As a consequence, the improvement of the impeller performance and noise are obtained from multi-objective optimization procedure.

Table 2.1. Comparison of calculated responses [7]

	Baseline	Optimized
pr_{tt}	2.0940	2.0944
η_{tt}	0.9137	0.9263
SPL_{in}(dB)	81.1406	76.5927
SPL_{out}(dB)	109.5489	109.5000

3. THEORETICAL BACKGROUND

3.1. COMPUTATIONAL FLUID DYNAMICS (CFD)

There are two basic approaches to analyze engineering systems involving fluid flow: experimental and numerical. CFD is a field of study devoted to solution of governing equations of fluid flow. The main idea is to simulate real fluid flow by solving the incompressible or compressible Navier-Stokes equations using a numerical method implemented on a powerful computer. Computational Fluid Dynamics is now routinely used to analyze the fluid flows.

CFD solutions are not guaranteed to be physically meaningful. If the grid is not properly applied or if the boundary conditions and flow parameters are not properly specified, the obtained results may not be physically correct. Therefore, if it is possible, experimental validation is highly recommended to determine if the computer output is meaningful.

In this study, numerical analyses are performed using a commercial CFD solver Fluent which employs the finite volume method (FVM). In FVM, the conservation principles are applied to each control volume to yield a set of algebraic equations. These algebraic equations are then solved numerically to obtain unknown quantities. All quantities at the center of the each control volume are averaged over the control volume.

3.1.1. Governing Equations

CFD is fundamentally based on the governing equations of fluid dynamics. The following physical laws are adopted [8]:

- Mass is conserved for the fluid

- The rate of change of momentum equals the sum of forces acting on the fluid (Newton's second law)

- The rate of change of energy equals the sum of rate of heat addition to and the rate of work done on the fluid (First law of thermodynamics)

For steady, incompressible, laminar flow of Newtonian fluid, the continuity and momentum equations can be written as follows:

$$\vec{\nabla}.\vec{u} = 0 \tag{3.1}$$

$$(\vec{\nabla}.\vec{u})\vec{u} = -\frac{1}{\rho}P' + v\nabla^2\vec{u} \tag{3.2}$$

where u is the velocity of the fluid, ρ is the density, and υ is its kinematic viscosity. Both ρ and υ are assumed to be constant. The gas is at low Mach number enough to behave as an incompressible fluid for many gas flows. Since $\vec{u} = u_i + u_j + u_k$, for a three dimensional flow in Cartesian coordinates, there are four coupled differential equations and four unknowns: u_i, u_j, u_k and P'.

Compared to laminar flow simulations, turbulent flows are more challenging to model because additional equations are solved. The reason is that all turbulent flows contain unsteady, three-dimensional, swirling, vortical structures called turbulent eddies of various sizes. Mathematical models are employed to take into account mixing and diffusion caused by turbulent eddies. For steady, incompressible, and turbulent flow, the Reynolds-averaged Navier-Stokes (RANS) equation is derived as follows:

$$\frac{\partial u_i}{\partial x_i} = 0 \tag{3.3}$$

$$\rho\left(u_i\frac{\partial u_j}{\partial x_i}\right) = -\frac{\partial P}{\partial x_j} - \frac{\partial \tau_{ij}}{\partial x_i} + \rho g_j \tag{3.4}$$

Velocity is decomposed into mean and fluctuating parts:

$$u_i = \bar{u}_i + u_i'$$ (3.5)
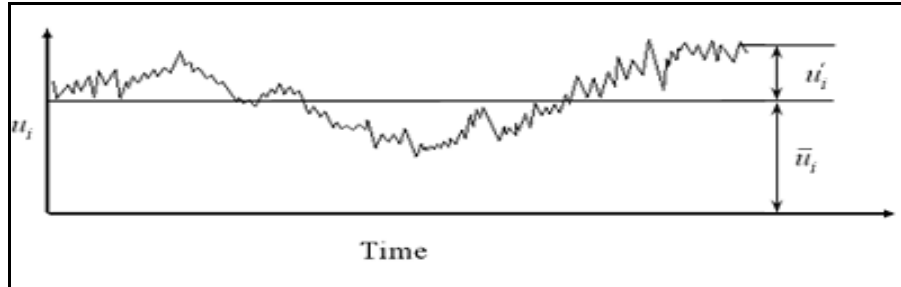
Figure 3.1. Decomposition of velocity

where the prime indicates a fluctuating velocity component and the overbar denotes the time average ($\bar{u}_i = \dfrac{1}{T}\displaystyle\int_0^T u_i dT$). After substituting decomposed velocity and taking the time average, the continuity and momentum equation becomes:

$$\frac{\partial \bar{u}_i}{\partial x_i} = 0$$ (3.6)

$$\rho\left(\bar{u}_i \frac{\partial \bar{u}_j}{\partial x_i}\right) = -\frac{\partial P}{\partial x_j} - \frac{\partial}{\partial x_i}\left(\overline{\rho u_i' u_j'}\right) - \frac{\partial \tau_{ij}}{\partial x_i} + \rho g_j$$ (3.7)

The term τ_{ij} shown above is a viscous stress tensor that represents momentum transport due to molecular motion. The additional Reynolds stress term $\overline{\rho u_i' u_j'}$ represents momentum transport due to turbulence and is assumed to be proportional to the turbulent viscosity μ_T and shear rate according to hypothesis known as the generalized Boussinesq hypothesis. The hypothesis introduces a new variable, k, the kinetic energy of turbulence.

$$\overline{\rho u_i' u_j'} = \mu_T\left(\frac{\partial \bar{u}_i}{\partial x_j} + \frac{\partial \bar{u}_j}{\partial x_i}\right) - \frac{2}{3}\delta_{ij}\rho k$$ (3.8)

The problem of Reynolds decomposition and averaging is that it introduces additional variables (fluctuating velocities), for which there are no available relations. Therefore, additional empirical equations are devised by turbulence models.

3.1.2. Turbulence Modeling

Turbulent flows may be computed using several approaches. The main approaches are either solving the Reynolds averaged Navier-Stokes (RANS) equations with appropriate models for turbulent quantities or computing fluctuating quantities directly.

Turbulent flows are characterized by a wide range of length scales. Think of turbulent flow as a collection of eddies of different sizes. RANS-based approaches attempt to model all scales of turbulence. These turbulence approaches are of an empirical nature. They contain constants which are to be selected so that experimental results agree as much as possible with CFD calculations in the investigated geometry and flow regime. No turbulence model is universally valid, meaning that it is not guaranteed to yield a physically correct solution for all applications.

There are many RANS models including algebraic, one-equation, two-equation, and Reynolds stress models. Most turbulence models are based on the concept of the turbulent (eddy) viscosity μ_T which is defined as a function of characteristic velocity u_c, and characteristic length scale l_c of turbulent eddies. These turbulence models are known as eddy viscosity models.

$$\mu_T = \rho u_c l_c \tag{3.9}$$

Eddy viscosity models can be classified by the number of transport equations employed. These transport equations are solved simultaneously with continuity and momentum equations.

Algebraic turbulence models (or zero-equation models) assume that the eddy viscosity depends on the local flow quantities such as velocity gradients and on a given length scale for the energy carrying vortices [9]. No differential equations are solved for

turbulence quantities because this dependence is expressed by algebraic equations. For a limited range of flows such as jets and wake flows, it is possible to specify turbulent viscosity and apply algebraic turbulence models. Algebraic turbulence models consume less computational effort.

One-equation turbulence models solve a single partial differential equation for the velocity scale of the turbulence. This conservation equation includes convective and diffusive transport terms, as well as the production and dissipation of eddy viscosity. One-equation models are relatively less popular because it is weak for separated flows, free shear flows, and decaying turbulence.

Two-equation turbulence models use two transport equations for both characteristic velocity and length scale. The most popular k-ε and k-ω model belongs to this model. Most often one of the transport variables is the turbulent kinetic energy k. Common choices for the second transport variable are the turbulent dissipation ε, and the specific dissipation ω. The first variable k determines the energy in the turbulence and the second variable determines the scale of the turbulence. The standard k-ε model was developed in the early 1970s. Many attempts have been made to develop standard k-ε. As a result of this interest, various similar turbulence models including k-ω are introduced. The well-known two-equation models are listed below:

k-ε models

– Standard k-ε model

– Realizable k-ε model

– RNG k-ε model

– Low-Reynolds k-ε model

k-ω models

– Wilcox's k-ω model

– Wilcox's modified k-ω model

– Shear stress transport(SST) k-ω model

3.1.2.1. The k-ε Model

The k-ε turbulence model is a semi empirical model based on modal transport equations for k and ε. The turbulence kinetic energy k is defined as the variance of the fluctuations in velocity and the turbulence dissipation ε is defined as the rate at which the velocity fluctuations dissipate. The k-ε is only valid for fully turbulent flows because in the derivation of model, it is assumed that the effects of molecular viscosity are negligible.

The k-ε assumes that the eddy viscosity is linked to turbulence kinetic energy k and dissipation rate ε by the relation in Equation 3.10.

$$\mu_T = c_\mu \rho \frac{k^2}{\varepsilon} \tag{3.10}$$

where c_μ is a constant and its value is 0.09 for the standard k-ε model. The values of k and ε come directly from the differential model transport equations for the turbulence kinetic energy and dissipation as shown in Equation 3.11 and Equation 3.12 [10].

$$\frac{\partial \rho k}{\partial t} + \frac{\partial \rho u_i k}{\partial x_i} = \frac{\partial}{\partial x_j}\left[\left(\mu + \frac{\mu_T}{\sigma_k}\right)\frac{\partial k}{\partial x_j}\right] + G_k + G_b - \rho\varepsilon \tag{3.11}$$

$$\frac{\partial \rho \varepsilon}{\partial t} + \frac{\partial \rho u_i \varepsilon}{\partial x_i} = \frac{\partial}{\partial x_j}\left[\left(\mu + \frac{\mu_T}{\sigma_\varepsilon}\right)\frac{\partial \varepsilon}{\partial x_j}\right] + c_{\varepsilon 1} + (G_k + c_{\varepsilon 3}G_b)\frac{\varepsilon}{k} - c_{\varepsilon 2}\rho\frac{\varepsilon^2}{k} \tag{3.12}$$

where the modal constants $c_{\varepsilon 1}$=1.44, $c_{\varepsilon 2}$=1.92, $c_{\varepsilon 3}$=0-1, σ_k=1 and σ_ε=1.3. These values have been determined from experiments for fundamental turbulent shear flows. G_k is the generation of turbulence kinetic energy due to the mean velocity gradients. G_b represents the generation of turbulence kinetic energy due to buoyancy. G_k and G_b are computed as follows:

$$G_k = -\rho \overline{u_i' u_j'} \frac{\partial u_j}{\partial x_i} = \mu_T \frac{\partial u_j}{\partial x_i} \tag{3.13}$$

$$G_b = \beta g_i \frac{\mu_T}{Pr_t} \frac{\partial T}{\partial x_i} \tag{3.14}$$

where Pr_t is the turbulent Prandtl number that has a default value of 0.85 for the standard and realizable k-ε model.

The RNG k-ε model was developed using Re-Normalization Group (RNG) approach. The RNG approach is a mathematical technique that can be used to renormalize Navier-Stokes equations resulting in an additional term in ε equation. In standard k-ε model the eddy viscosity is calculated from a single turbulence length scale but actually all scales of motion contribute to the turbulent diffusion. The effects of different scales of motion through changes to the production term are attempted to provide in the RNG k-ε model.

3.1.2.2. The k-ω Model

The k-ω model is an empirical model based on transport equations for the turbulence kinetic energy k and the specific dissipation rate ω. The model does not include the complex non-linear damping functions required for the k-ε model and hence captures the flow near the walls more accurately for low-Reynolds number computations.

The k-ω turbulence model assumes that the eddy viscosity is linked to k and ω via the relation in Equation 3.15.

$$\mu_T = \alpha^* \frac{\rho k}{\omega} \qquad (3.15)$$

where k and ω are obtained from the following transport equations [11]:

$$\frac{\partial \left(\rho u_j k \right)}{\partial x_j} = P_k - \beta^* \rho \omega k + \frac{\partial}{\partial x_j} \left[\left(\mu + \frac{\mu_T}{\sigma_k} \right) \frac{\partial k}{\partial x_j} \right] \qquad (3.16)$$

$$\frac{\partial \left(\rho u_j \omega \right)}{\partial x_j} = \alpha \frac{\omega}{k} P_k - \beta \rho \omega^2 + \frac{\partial}{\partial x_j} \left[\left(\mu + \frac{\mu_T}{\sigma_\omega} \right) \frac{\partial \omega}{\partial x_j} \right] \qquad (3.17)$$

In these equations, P_k represents the production of kinetic energy. For incompressible flows it is expressed by

$$P_k = \mu_T \left(\frac{\partial u_i}{\partial x_j} + \frac{\partial u_j}{\partial x_i} \right) \frac{\partial u_i}{\partial x_j} \qquad (3.18)$$

In standard k-ω model, the modal constants α^*=1, β^*=0.09, α=5/9, β=0.075, σ_ω=2 and σ_k=2.

3.1.3. Computation of Fluctuating Quantities

3.1.3.1. Direct Numerical Simulation (DNS)

DNS involves the numerical solution of the equations that govern fluid flow without any turbulence model. This means that all turbulent phenomena at all time and length scales are resolved by solving Navier-Stokes and continuity equation. The smallest length, time and velocity scales need to be acquired because for a successful simulation, whole scales of the turbulence including the smallest dissipative scales must be resolved. This data can be obtained by applying Kolmogorov turbulence theory. The Kolmogorov length scale η and velocity scale are given by

$$\eta = \left(\frac{\upsilon^3}{\varepsilon} \right)^{\frac{1}{4}} \qquad (3.19)$$

$$\vartheta = \left(\upsilon \right)^{\frac{1}{4}} \qquad (3.20)$$

where υ is the kinematic viscosity and ε is the rate of kinetic energy dissipation. Assuming U is the mean velocity and L is the integral length scale and noting ε=U³/L, required number of grid points for a three-dimensional DNS is calculated as follows:

$$\left(\frac{L}{\eta} \right)^3 \approx \left(\frac{L\varepsilon^{1/4}}{\upsilon^{3/4}} \right)^3 \approx \left(\frac{LU^{3/4}}{\upsilon^{3/4}L^{1/4}} \right) \approx \left(\text{Re}^{3/4} \right)^3 \approx \text{Re}^{9/4} \qquad (3.21)$$

The number of time steps required to simulate the entire flow is T/Δt where T is the time scale of the largest eddy and Δt is the time step. Noting $\Delta t = \eta / \vartheta$, the number of time steps is obtained as shown in Equation 3.22.

$$\frac{T}{\Delta t} = \frac{L\vartheta}{\eta U} = \frac{L(\varepsilon)}{U\upsilon^{3/4}/\varepsilon^{1/4}} = \mathrm{Re}^{1/2} \tag{3.22}$$

The number of grid points and time steps grows as a power of Reynolds number. Therefore, the computational resource required by a DNS is very high. For the Reynolds number encountered in most applications, the computational demand would exceed the capacity of the computers available today. DNS is generally useful for flows at Re=10^3-10^4.

3.1.3.2. *Large-Eddy Simulation (LES)*

LES comes between the RANS and the DNS approaches in terms of computational effort. Turbulent flows are characterized by eddies with a wide range of length and time scales. In LES, large eddies are resolved directly while small eddies and their interaction with large eddies are modeled. This decomposition is illustrated in Figure 3.2. The distribution of the turbulent kinetic energy is described by the energy spectrum *E(k)* as a function of associated wave number *k* which is proportional to the velocity fluctuation frequency. Small eddies have higher frequencies, thus higher wave numbers, than large eddies.
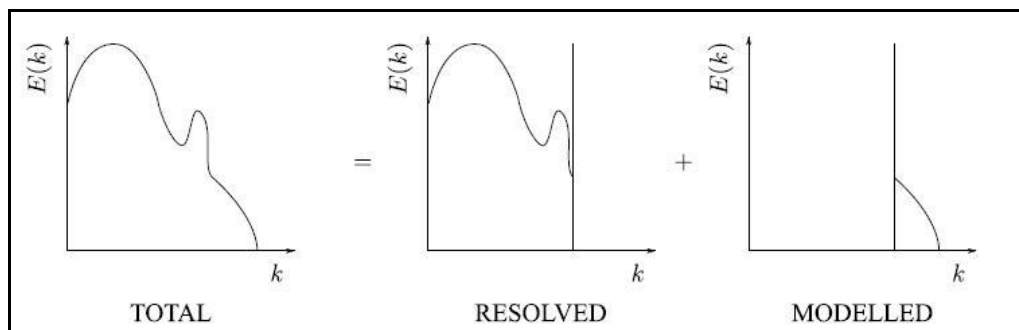
Figure 3.2. Decomposition of the energy spectra in LES

The idea behind the LES model is that the large scale eddies of a large Reynolds number flow are numerically calculated with reasonable accuracy from the LES governing equations of fluid dynamics. On the other hand, the small scale eddies are modeled via sub-grid scales resulting from space filtering the Navier-Stokes equations [12]. Resolving

only the large eddies allows us to use coarser mesh in LES than in DNS but the required mesh is still finer in LES than typically used in RANS.

The turbulence models computing fluctuating quantities can resolve shorter length scales than RANS models. Hence LES and DNS have clear superiority over RANS methods for the simulation of complex flows. On the other hand, RANS can determine mean flow accurately with a demand of much lower computational power in many engineering applications. The schematic comparison of basic CFD methods is illustrated in Fig. 3.3.
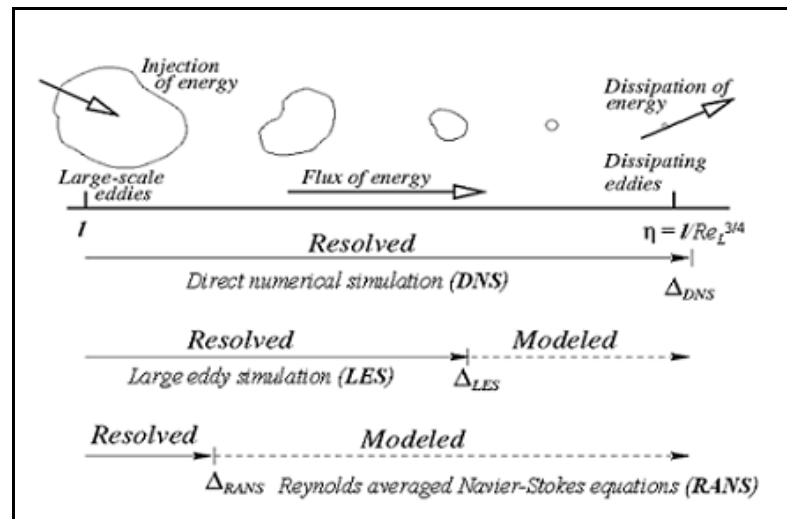
Figure 3.3. Comparison of basic CFD approaches

3.1.4. Grid Generation

Grid generation is considered as the most important and time consuming step in a CFD solution. A grid defines the cells on which flow variables such as velocity and pressure are calculated throughout the computational domain by solving discretized versions of the conservation equations [13]. Therefore, the quality of the grid influences the quality of the simulation directly. Additionally, it is much harder for the numerical scheme to converge to the physical solution with low-quality coarse grids. The criteria of poor grid quality are listed below [14]:

- high degree of skewness
- abrupt changes in grid spacing
- insufficient resolution to resolve proper physical length scales
- grid topology poorly suited to sufficiently cover the flow physics
- grid lacking special features needed by physical submodels
- grid with nonsingularity

Structured, unstructured and hybrid computational grids are in use today. Hybrid grids contain both unstructured and structured elements. These elements are used according to their strength and weaknesses to take advantage of the positive features of both unstructured and structured grids.

3.1.4.1. Structured Grid

A structured grid consists of quadrilateral elements in 2-D and hexahedral elements in 3-D (Fig. 4). These elements cover the calculation domain in a regular repeating pattern.
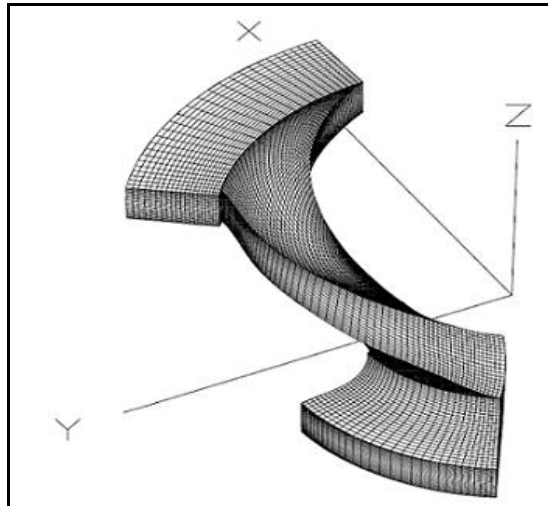
Figure 3.4. Structured grid of a rotor channel

The grid has a significant impact on rate of convergence, solution accuracy and CPU time required. The generated CFD grid must be dense enough to obtain accurate numerical results, but it cannot be so dense because memory requirements make the solution impractical to obtain.

The mesh adjacent to the wall should be fine enough to capture all relevant flow features in boundary layer. Hexahedral and quadrilateral elements are preferred in boundary layers because they are very efficient at filling space. This allows the user to control grid points freely. Because the user interactively positions the elements, points can be refined in high gradient regions of the calculation field and gradually expand out to a less dense from these regions. Cell aspect ratio, which is ratio of longest edge length to shortest edge length, should be near one for a high quality grid where flow is multi-dimensional. In addition, hexahedral elements give more accurate results for the same number of control volumes.

The major drawbacks of structured grids are time and flexibility. Manual creation of block structures is generally more time consuming and offer little flexibility for complex geometries compared to unstructured meshes.

3.1.4.2. Unstructured Grid

The cells are arranged in an arbitrary fashion to fill the computational domain. Because the arrangement of elements has no regular repeating pattern, the grid is called unstructured. These types of grids fill the calculation domain by triangle elements in 2-D and tetrahedral elements in 3-D (Fig. 5), without generating continuous grid lines.
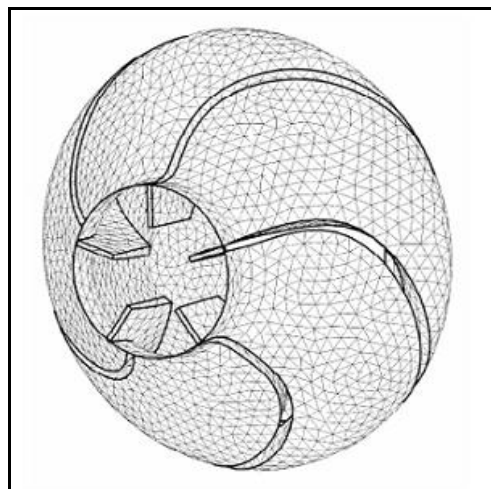
Figure 3.5. Unstructured grid of a pump diffuser

The advantage of unstructured grid is that they require little user time and effort even inexperienced users can generate valid mesh by using meshing software. Unlike structured grid, unstructured grid gives a lot of flexibility in mesh generation and enables the solution of very complex geometries in a relatively short time.

The major disadvantages of unstructured grid are indefinite data structure and limited user control when generating mesh. Their data structure is more complex and the calculation time increases considerably as compared to structured grids. The user control is generally limited to the boundaries because mesh generating software fills interior regions automatically. This is causing a problem and resulting in finer entire computational grid in order to obtain desired mesh density in a local area. Another drawback is memory requirement when post processing the solution. Interpolating the results onto planes and surfaces requires longer execution time in comparison to structured grid.

3.2. BASICS OF ACOUSTICS

Sound is defined as periodic mechanical vibrations of a medium by means of which sound energy is carried through that medium. Sound is a periodic process and involves energy transport.

Sound waves in fluids are often produced by vibrating solid surfaces in the fluid. As the vibrating surface moves, the fluid adjacent to the surface is compressed or rarefied. Particles of the medium are excited into oscillation about their usual position of rest resulting in pressure fluctuations moving outward from the vibrating surface as a sound wave. The propagation of sound involves energy transfer but it does not cause the transport of matter.

3.2.1. Sound Pressure, Power & Intensity Level

Decibel is a logarithmic unit of measurement that expresses the magnitude of physical quantity relative to a specific reference level. Decibel (dB) is used for many measurements in acoustics such as sound intensity and power level etc. because human

ears perceive sounds in logarithmic scale instead of in both frequency and amplitude domain.

Sound intensity is defined as the sound power per unit area. Since sound wave is three-dimensional quantity and occupies space, it is useful to characterize the rate of energy transfer with respect to area. The sound intensity level (SIL) is expressed in decibel as:

$$SIL = 10\log_{10}(I/I_{ref})$$ (3.23)

where I is the actual sound intensity and I_{ref} is the reference intensity (10^{-12} W/m^2).

Sound power is the energy of sound per unit of time. The sound power level is a measure of the total power radiated in all directions by a sound source. The sound power level (L_w) of a signal with a sound power W and threshold of hearing 10^{-12} W as a reference power W_{ref} is:

$$L_w = 10\log_{10}(W/W_{ref})$$ (3.24)

The sound intensity is one way of measuring amplitude of a sound wave at a point. However, pressure is commonly used as a measure of the amplitude of the sound wave because pressure is easier to measure. Sound pressure level (SPL) is a logarithmic measure of the sound pressure of a sound relative to a standard reference value and defined as:

$$SPL = 20\log_{10}(P/P_{ref})$$ (3.25)

where P_{ref} represents the threshold of hearing at 1 kHz and has a value of 20 μPa.

3.3. AEROACOUSTIC BACKGROUND

A general theory for the mechanism of flow induced noise generation by a turbulent shear flow was first formulated by Lighthill in his 1952 paper [15]. The influence of solid boundaries was investigated by Curle [16]. Ffowcs Williams and Hawkings [17] extended

the Lighthill-Curle theory of aerodynamic sound to incorporate the effect of surfaces in arbitrary motion. The equation that has become associated with their names is an exact rearrangement of the continuity equation and the Navier-Stokes equations into the form of an inhomogeneous wave equation.

3.3.1. Lighthill's Analogy and FW-H Formulation

Lighthill provided a theoretical basis to the understanding of the radiation of the sound generated by a turbulent flow with his acoustics analogy. The analogy is based on the hypothesis that the part of the flow field which is the source for acoustics is distinct, so that the acoustic waves do not interfere with the flow. Lighthill rewrote the Navier-Stokes equations into an exact, inhomogeneous wave equation and identified the inhomogeneous terms as acoustic sources [18]. Lighthill's equation can be written as follows:

$$\frac{\partial^2 \rho}{\partial t^2} - c_0^2 \nabla^2 \rho = \frac{\partial^2 T_{ij}}{\partial x_i \partial x_j} \tag{3.26}$$

Lighthill turbulence stress tensor is expressed by $T_{ij} = \rho u_i u_j - \sigma_{ij} + \left(p - c_0^2 \rho \right) \delta_{ij}$ where δ_{ij} is the Kronecker delta function and σ_{ij} is the viscous stress tensor.

The main disadvantage of Lighthill's acoustic analogy is its limitation to problems where solid surfaces do not play a major role in sound generation.

Ffowcs Williams and Hawkings (FW-H) proposed an extension of Lighthill's acoustic analogy that includes the influence of arbitrary moving surfaces on sound generation. The FW-H equation can be obtained as inhomogeneous wave equation by taking time derivative of the generalized continuity equation, subtracting the divergence of the generalized momentum equation, and then rearranging terms. The FW-H equation is given by

$$\frac{\partial^2 \rho'}{\partial t^2} - c_0^2 \frac{\partial^2 \rho'}{\partial x_i^2} = \frac{\partial^2}{\partial x_i \partial x_j} \left(T_{ij} H(f) \right) + \frac{\partial}{\partial x_i} \left(\sigma'_{ij} \delta(f) \frac{\partial f}{\partial x_j} \right) + \frac{\partial}{\partial t} \left(\rho_0 V_{si} \delta(f) \frac{\partial f}{\partial x_i} \right) \tag{3.27}$$

This equation has two surface source terms and a volume source term. Source terms are defined as follows [19]:

- quadrupole source $\partial^2/\partial x_i \partial x_j \left(T_{ij} H(f) \right)$: is a volume distribution due to flow outside the surfaces

- dipole source $\partial/\partial x_i \left(P'_{ij} \delta(f) \partial f/\partial x_j \right)$: is a surface distribution due to the interaction of the flow with the moving bodies

- monopole source $\partial/\partial t \left(\rho_0 V_{si} \delta(f) \partial f/\partial x_i \right)$: is a surface distribution due to the volume displacement of fluid during the motion of surfaces.

The main contribution to the noise generated by fans is due to steady and unsteady forces exerted by moving surfaces. The quadrupole source term represents nonlinear effects and its contribution is insignificant in many subsonic applications. The three source terms in the FW-H equation have obvious physical meaning, and so insignificant terms do not have to be computed numerically at all times.

3.3.2. Vortex Sound

The vortex sound theory introduced by Powell (1964) and Howe (2002) is an alternative to Lighthill's analogy. According to the vortex sound theory, the presence of vorticity is responsible for sound generation in a flow field in subsonic homentropic flows. This theory expresses noise generation as a function of velocity and vorticity fields [20]:

$$\left(\frac{D}{Dt}\left(\frac{1}{c^2}\frac{D}{Dt} \right) - \frac{1}{\rho}\nabla.\left(\rho\nabla \right) \right) B = \frac{1}{\rho}div\left(\rho\omega \wedge v \right) \qquad (3.28)$$

where D is the total derivative, c is speed of sound in the flow region, B is the total enthalpy, v is the velocity and ω is the vorticity. In this equation it is stated that there is no sound generation in an irrotational flow (ω=0).

3.4. DESIGN OF EXPERIMENT

Design of experiment (DOE) is an organized method that is used to determine the relationship between the different factors affecting a process and the output of that process. All relevant factors are varied systematically according to DOE approach to identify optimal conditions, the factors that most affect the results and the existence of interactions between factors when the results of runs are analyzed.

The main objective of DOE is the selection of the points where response should be evaluated. This selection has a large influence on the accuracy of the approximation because DOE methods require well-structured data matrices to find a suitable mathematical model for the investigated process. DOE methodology provides a predictive knowledge of a complex, multi-variable process with fewest trials possible and thus helps to reduce optimization costs.

Factorial design, Taguchi method and response surface design are the major approaches to DOE. Factorial design is the simplest design to create but it is often inefficient because each factor tested at each condition of the factor results in large number of runs. Taguchi method reduces the number of runs as compared to a factorial design but ignores interactions between parameters. Response surface method is adopted in this study, and a detailed description will be given only for response surface design.

The most important part before applying the response surface methodology is the selection of proper DOE strategy that has a large effect on the building of response surface. The choice of a DOE methodology depends on the objectives of the problem and the number of factors to be investigated. The common DOE strategies are central composite design and Box-Behnken design.

3.4.1. Response Surface Methodology

Response surface methodology (RSM) is a collection of statistical and mathematical techniques useful for developing, improving and optimizing processes in which a response of interest is influenced by several variables and the objective is to optimize this response

[21]. RSM was originally developed to model experimental responses, and then migrated into the modeling numerical applications. The difference is in the type of error generated by the response.

In general, the relationship between the response y and independent variables $x_1, x_2, \ldots, x_k$ can be expressed as

$$y = f(x_1, x_2, \ldots, x_k) + \varepsilon \qquad (3.29)$$

where ε represents the error in the response y. The surface represented by $f(x_1, x_2, ., x_k)$ is called a response surface. The variables $x_1, x_2, \ldots, x_k$ are independent and the response y depends on them.

In most RSM problems, the relationship between the response and the independent variables is unknown. Therefore, a suitable approximation to the true relationship must be found as a first step of RSM. Usually, a low order polynomial (first order and second order) is appropriate. If the response can be defined properly by a linear function of independent variables, then the approximating function is called a first order model. A first order model with two independent variables can be expressed as

$$y = \beta_0 + \beta_1 x_1 + \beta_2 x_2 + \varepsilon \qquad (3.30)$$

If the curvature in the response surface is strong enough, a higher degree polynomial should likely be used because the first-order model remains inadequate. For the case of two independent variables, the second-order model is

$$y = \beta_0 + \beta_1 x_1 + \beta_2 x_2 + \beta_{11} x_{11}^{2} + \beta_{22} x_{22}^{2} + \beta_{12} x_1 x_2 + \varepsilon \qquad (3.31)$$

The second order model is widely used in response surface methodology for several reasons [21]:

- The second-order model is very flexible. It can take on a wide variety of functional forms, so it will often work well as an approximation to the true response surface.

- It is easy to estimate the parameters in the second order model. The method of least squares can be used for this purpose.

- There is considerable practical experience indicating that second order models work well in solving real response surface problems.

The main objective of RSM is to find the optimum response. It is important to find the compromise optimum that does not optimize only one response when problem includes more than one response. Hence it is necessary to understand how the response changes depending on the design variables. In general, response surface can be visualized graphically to see the shape of a response surface. An example of response surface plot is illustrated in Figure 3.6.
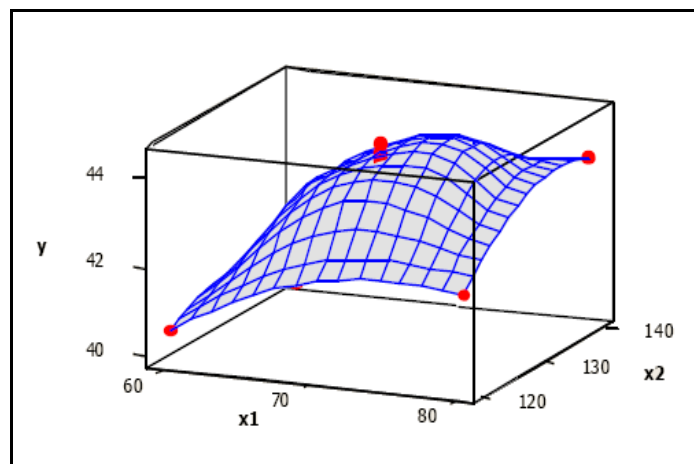
Figure 3.6. Response surface plot

3.4.2. Central Composite Design

Central composite design (CCD) is widely used for estimating second order response surfaces. This design requires five levels for each factor. CCD consists of three types of points: cube points, axial points and centre points (Fig.3.7) [22]. Therefore total number of runs needed can be determined as follows:

$$N = 2^k + 2k + c_0 \tag{3.32}$$

where k is the number of factors and c_0 is the number of center points that are used to calculate experimental error.

The distance between axial points and the center points is denoted by α and is linked to the number of factors by the relation in Equation 3.33.

$$\alpha = \left[k \right]^{1/4} \tag{3.32}$$

The axial points establish new extremes for the low and high levels for all factors. By using the formula shown above, α can be calculated easily for 6 factors. It has a value of 2.828. CCD is not adopted for this study because α of 2.828 makes blade number rational in several runs.
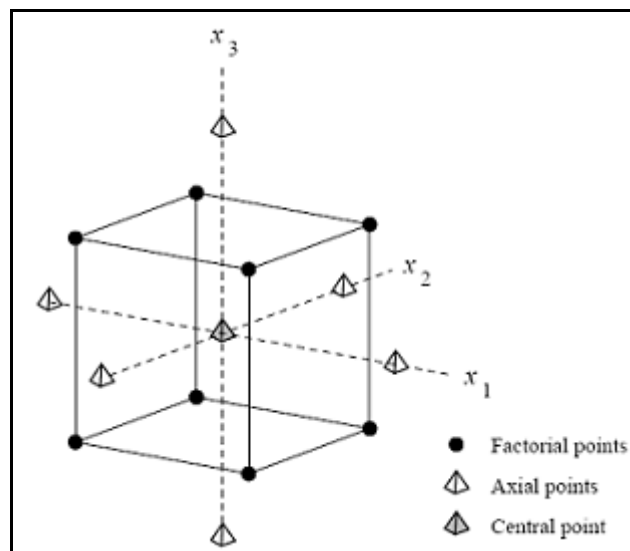
Figure 3.7. Central composite design for 3 design variables

3.4.3. Box-Behnken Design

Box-Behnken design (BBD) is constructed by first combining two-level factorial designs with incomplete block designs and then adding a specified number of replicated center points [23]. Unlike CCD, the treatment combinations are at the midpoints of edges of the design space and at the center (Fig.3.8).
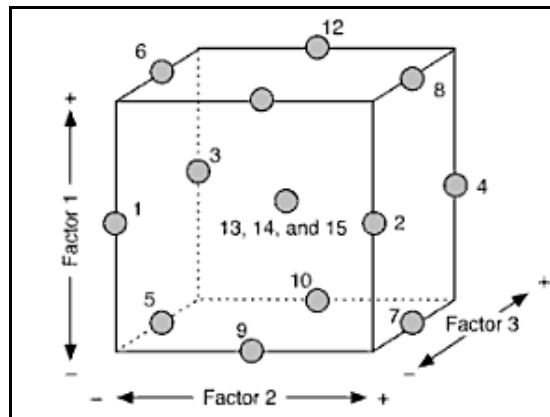
Figure 3.8. Box Behnken design for 3 design variables

Box-Behnken is an alternative to a central composite design approach when estimating the first and second order terms of a response surface. BBD alternative is useful when the corners of the cubic portion are not necessary for response surface exploration and observations at only three levels are desired. BBD requires only three levels of each variable, as opposed to five for the CCD and hence avoids physical constraints for this study. This is the main reason of using Box-Behnken design approach.

Both CCD and BBD are much more efficient in comparison to 3^k factorial designs in terms of the number of combinations necessary to solve complete second-order polynomial models.

Table 3.1. Comparison of second-order designs in terms of number of runs

# of factors	3^k factorial	Central-Composite	Box-Behnken
2	9	13	-
3	27	20	15
4	81	31	27
5	243	32	46
6	729	53	54

4. PRELIMINARY STUDY: 2-D MULTI-OBJECTIVE PUMP OPTIMIZATION

Design of experiment (DOE) optimization study based on flow field simulations was first carried out on radial flow pump with a 2-dimensional approach. The aim is the maximization of the pump performance and minimization of the generated noise by adjusting the blade's inlet and exit angles and impeller's inlet and outlet diameters. This study shows the influence of geometrical parameters on the turbomachinery performance which must be considered before employing an effective 3-dimensional optimization.

The baseline impeller has 7 backward curved blades with inlet and outlet diameter D_1, D_2 and inlet and exit angles β_1, β_2. The blade thickness is constant. The geometrical configuration of casing was kept constant to eliminate the effect of it.
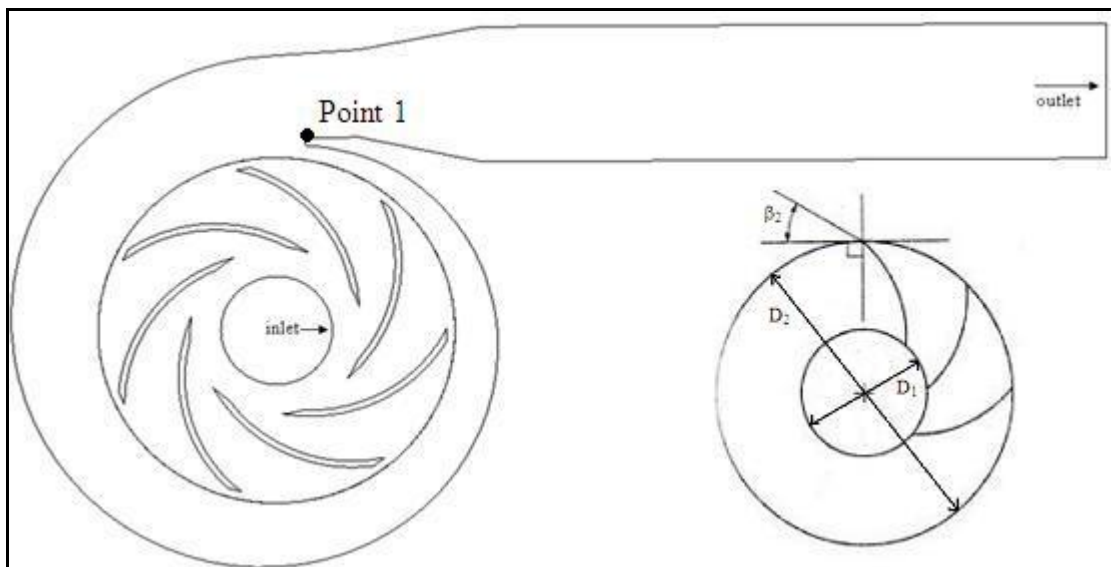
Figure 4.1. The baseline configuration of radial pump

4.1. NUMERICAL OPTIMIZATION METHODOLOGY

The factors of the blade's inlet and exit angles and impeller's inlet and outlet diameters are the most effective parameters on both hydrodynamic and hydroacoustic

performance. Therefore, these factors were chosen to vary in the optimization procedure. Ranges of the independent variables that were chosen according to baseline configuration are given in Table 4.1. After the design variables and their levels were set, the DOE matrix based on the central composite was created using Minitab software. The symbol "α" in Table 4.1 represents the distance from the center of the design space to a star point which establishes new low and high extreme values for each variable in the design.

Table 4.1. Chosen range of values for variable factors

Variable	Ranges				
	$-\alpha$	-1	0	1	$+\alpha$
inlet diameter(mm)	D_1-7	$D_1-3.5$	D_1	$D_1+3.5$	D_1+7
outlet diameter(mm)	D_2-7	$D_2-3.5$	D_2	$D_2+3.5$	D_2+7
inlet angle(°)	β_1-8	β_1-4	β_1	β_1+4	β_1+8
exit angle(°)	β_2-8	β_2-4	β_2	β_2+4	β_2+8

The design matrix shown in Table 4.2 consists of 31 sets of conditions including 7 replicates of center point. All 2-dimensional drawings and mesh generation and numerical simulations were carried out by the help of the journal files which includes a sequential list of commands. These commands were executed by Fluent and Gambit software. There is no need to simulate each replicate separately because numerical procedure is exactly the same and variation does not exist between replicates.

All the simulations of the pump were done in commercial CFD software Fluent. Unstructured computational grids were used for numerical simulations. The number of cells in a computational domain was around 80,000 for each one. Reynolds averaged Navier-Stokes (RANS) equation type of RNG k-epsilon turbulence model was adopted. Pressure-velocity coupling was achieved by SIMPLE algorithm provided by Fluent. A uniform flow with a rate of 0.574 kg/s and turbulent intensity of %2 was assigned at the inlet. At the outlet, outflow boundary condition was set. The rotational speed of the impeller was 2800 rpm. The other part, casing, was stationary.

Table 4.2. Design Matrix

Impeller #	D_1(mm)	D_2(mm)	β_1(°)	β_2(°)
1	D_1-3.5	D_2-3.5	β_1-4	β_2-4
2	D_1+3.5	D_2-3.5	β_1-4	β_2-4
3	D_1-3.5	D_2+3.5	β_1-4	β_2-4
4	D_1+3.5	D_2+3.5	β_1-4	β_2-4
5	D_1-3.5	D_2-3.5	β_1+4	β_2-4
6	D_1+3.5	D_2-3.5	β_1+4	β_2-4
7	D_1-3.5	D_2+3.5	β_1+4	β_2-4
8	D_1+3.5	D_2+3.5	β_1+4	β_2-4
9	D_1-3.5	D_2-3.5	β_1-4	β_2+4
10	D_1+3.5	D_2-3.5	β_1-4	β_2+4
11	D_1-3.5	D_2+3.5	β_1-4	β_2+4
12	D_1+3.5	D_2+3.5	β_1-4	β_2+4
13	D_1-3.5	D_2-3.5	β_1+4	β_2+4
14	D_1+3.5	D_2-3.5	β_1+4	β_2+4
15	D_1-3.5	D_2+3.5	β_1+4	β_2+4
16	D_1+3.5	D_2+3.5	β_1+4	β_2+4
17	D_1-7	D_2	β_1	β_2
18	D_1+7	D_2	β_1	β_2
19	D_1	D_2-7	β_1	β_2
20	D_1	D_2+7	β_1	β_2
21	D_1	D_2	β_1-8	β_2
22	D_1	D_2	β_1+8	β_2
23	D_1	D_2	β_1	β_2-8
24	D_1	D_2	β_1	β_2+8
25	D_1	D_2	β_1	β_2
26	D_1	D_2	β_1	β_2
27	D_1	D_2	β_1	β_2
28	D_1	D_2	β_1	β_2
29	D_1	D_2	β_1	β_2
30	D_1	D_2	β_1	β_2
31	D_1	D_2	β_1	β_2

4.2. RESULTS & DISCUSSION

The numerical simulations were done for unsteady case. A time step was set to $6*10^{-5}$ s, which corresponds to 1/360 of the period of the impeller motion. Maximum iterations of 20 were performed per time step. A point (Point 1 in Figure 4.1) on static volute tongue was determined and pressure data was obtained for each time step at this point. The simulations were run for 1080 time step (3 full rotation of impeller). Pressure data due to last rotation was only taken into account for optimization procedure because flow became completely statistically steady for each case after two rotations.

Table 4.3. CFD Results

#	impeller vorticity (1/s)	casing vorticity (1/s)	ΔP (Pa)	point_fft_1	point_fft_2
1	556.5	103.1	37807.2	205440.0	30693.8
2	551.7	103.6	37227.9	170256.8	30500.0
3	663.5	183.5	47175.4	974276.7	176778.7
4	652.1	181.4	46906.9	927708.6	191438.8
5	552.8	102.8	37980.2	200419.4	35386.7
6	541.4	102.4	37472.7	185081.4	21368.8
7	659.8	181.5	47375.0	980294.3	174112.5
8	649.0	179.1	47231.9	895713.1	175315.4
9	536.7	107.5	38605.0	235467.2	35358.2
10	521.9	107.0	38257.0	185879.4	18562.2
11	642.3	185.9	48104.8	1161479.2	219796.1
12	620.1	182.3	48273.7	1102259.5	208333.9
13	531.1	106.8	38730.6	241213.0	22667.3
14	507.9	106.6	38631.7	172104.8	40031.3
15	639.3	183.0	48209.8	1164610.3	217570.5
16	612.4	178.8	48566.1	1081928.2	197788.0
17	603.4	133.4	42725.0	473296.9	67184.6
18	581.9	130.2	42174.2	379383.5	81189.5
19	471.7	99.9	34088.4	95566.4	28556.2
20	666.4	221.7	54072.9	3021809.9	866762.3
21	595.9	133.2	42658.3	451759.8	68706.8
22	581.2	130.5	43096.0	448325.5	61557.4
23	624.9	127.2	41408.7	321502.6	67942.3
24	572.8	135.5	43707.0	481874.4	73080.2
25	592.9	131.2	42840.5	450483.2	62029.7

Based on simulation results, the key noise generation and performance details of average vorticity on surface, pressure difference between inlet and outlet, magnitude of power spectral density are considered and tabulated in Table 4.3. Only one of seven replicates of center point was simulated, hence there are 25 configurations can be seen in Table 4.3. The 2-dimensional domain consists of only two faces, impeller and casing. Average vorticity on these faces are used as an acoustical performance indicator.

The domain of the point pressure data is time. Frequency domain representations of the original data were obtained using Matlab which is capable of fast Fourier transform (FFT) operation. Magnitude of power spectral density was recorded at blade passing frequency (BPF) and its first harmonic (point_fft_1 and point_fft_2 in Table 4.3). Power spectral density describes how the energy of a signal is distributed with frequency and thus magnitude at BPF should be minimized. BPF varies with the number of blades and the rotational speed of impeller. It is equal to 326.7 Hz and can be calculated as follows:

$$BPF = \frac{n(rpm) * z}{60} = \frac{2800 * 7}{60} = 326.7 Hz$$

Figure 4.2 and 4.3 show the contours of static pressure. It can be seen that pressure is increasing in parallel with cross section of the casing.
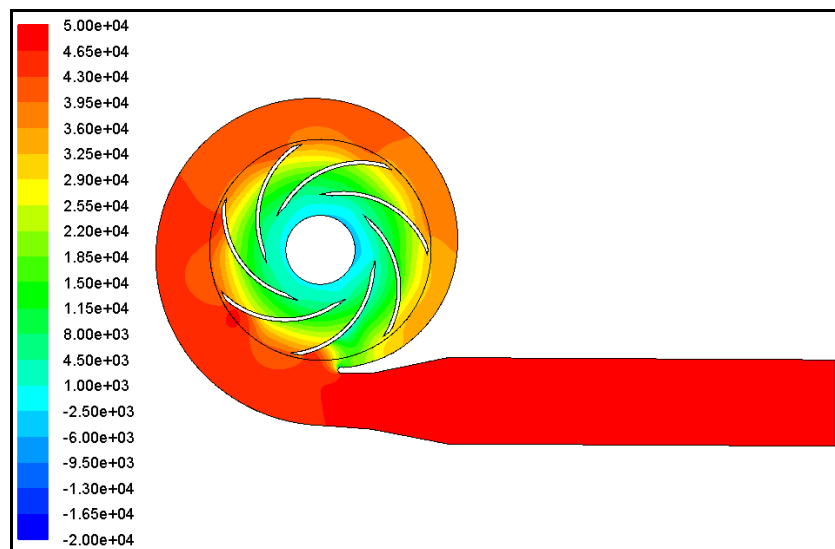
Figure 4.2. Contours of static pressure (geometry # 4)

Pressure difference between inlet and outlet (ΔP) is dramatically greater for geometry # 4 in comparison to # 14. Main difference between these two configurations is outlet diameter. It can be concluded that outlet diameter is the most influential parameter on ΔP. The gap between volute tongue and blades changes depending on outer diameter. Decreasing outer diameter increases the gap and results in reverse flows causing sudden pressure drops. These pressure drop zones can be seen more clearly around the tongue of geometry 14 which has less hydrodynamic performance with respect to geometry 4.
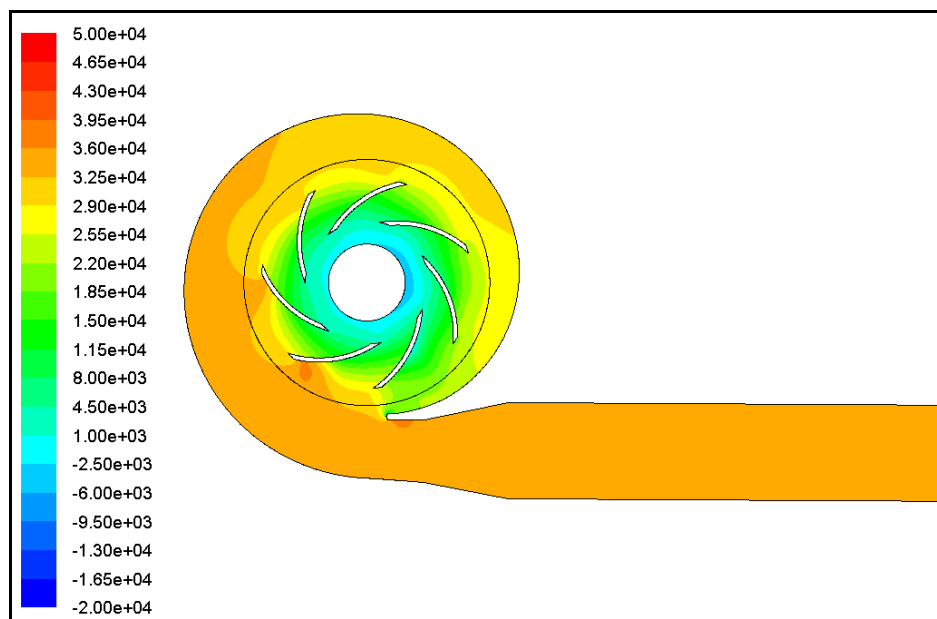
Figure 4.3. Contours of static pressure (geometry # 14)

There are five different response data available in Table 4.3. Only pressure difference between inlet and outlet is considered as hydrodynamic performance indicator. The others represent acoustical performance. The theory of a vortex sound suggests that the unsteady motion of vortices produces aerodynamic sound. Higher vorticity indicates strong disturbance in the flow and hence higher noise level. Although it is difficult to identify the detailed relationship between vorticity and aerodynamic noise, average vorticity on impeller and casing is desired to be as low as possible.

The vortex structures are mainly produced on the blades and then transported to whole flow domain. These structures contain high turbulent kinetic energy and degrade acoustical performance.
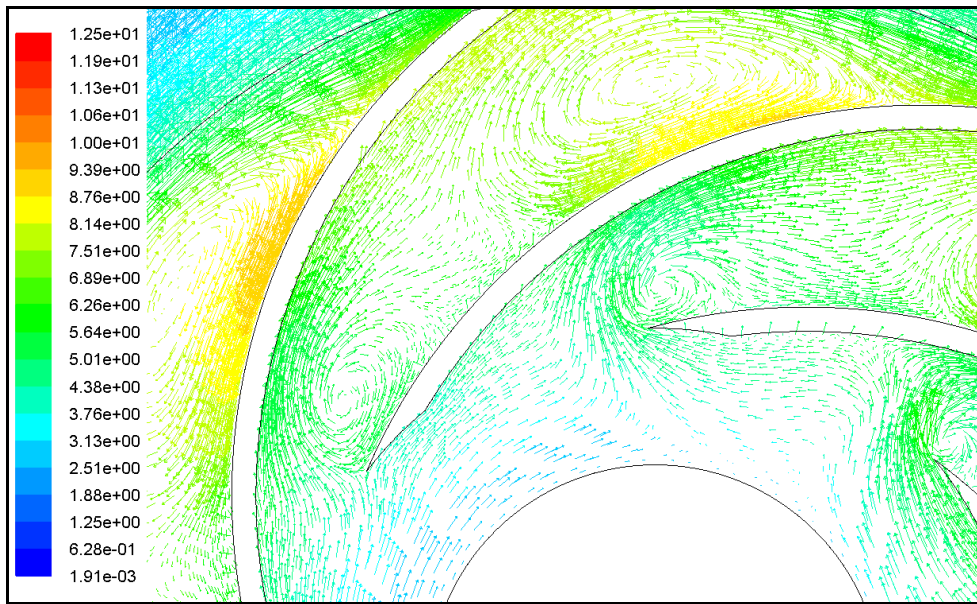
Figure 4.4. Relative velocity vectors between blades (geometry # 8)

Figures 4.4 and 4.5 illustrate relative velocity vectors along blade passage for pump configurations 8 and 24. Reverse flow patterns can be observed between blades. Although these patterns are similar in both two pumps, the disturbance is stronger in pump 8 because of the shorter distance between blades.
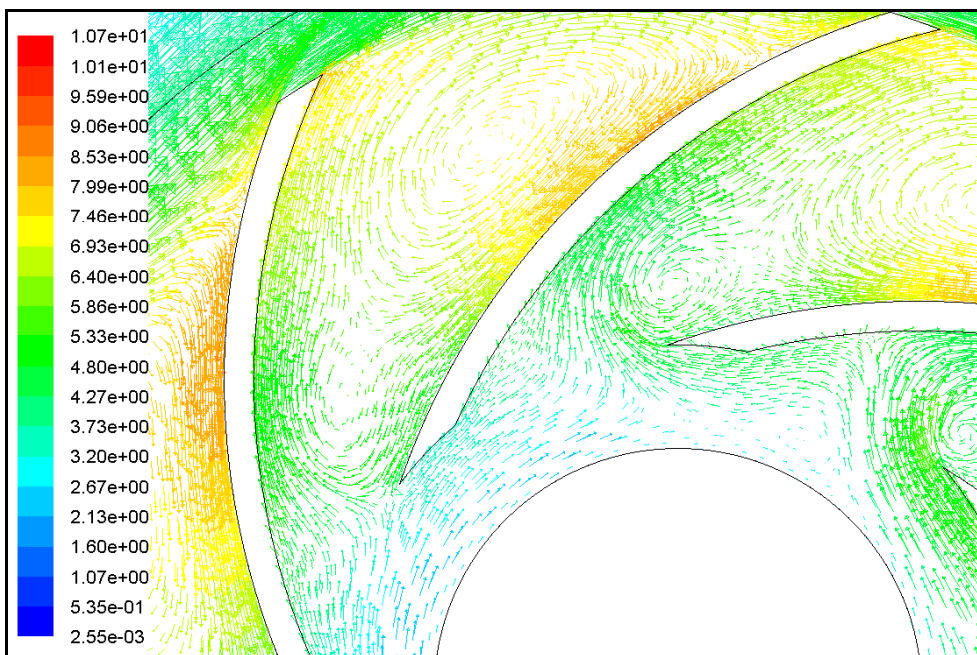
Figure 4.5. Relative velocity vectors between blades (geometry # 24)

The combination of input variables that optimize a set of responses is identified by using Minitab software. The optimization was accomplished by searching a combination that maximize ΔP and minimize the other responses. Optimal settings of the design variables were determined as D_1+7, D_2, β_1+8 and β_2+8. The comparison of baseline and optimal design is given in Appendix A (Table A.4).

The simulation of the optimized pump configuration was done with a similar manner. According to numerical simulations (Figure 4.6), the pareto design offers 5.7% less pressure increase in comparison to baseline. On the other hand, average vorticity on optimal impeller and casing are 14.1% and 25.3% less respectively. The reduction in ΔP is reasonable because pressure increase is still above the allowable minimum response value that was determined as a requirement for this response.
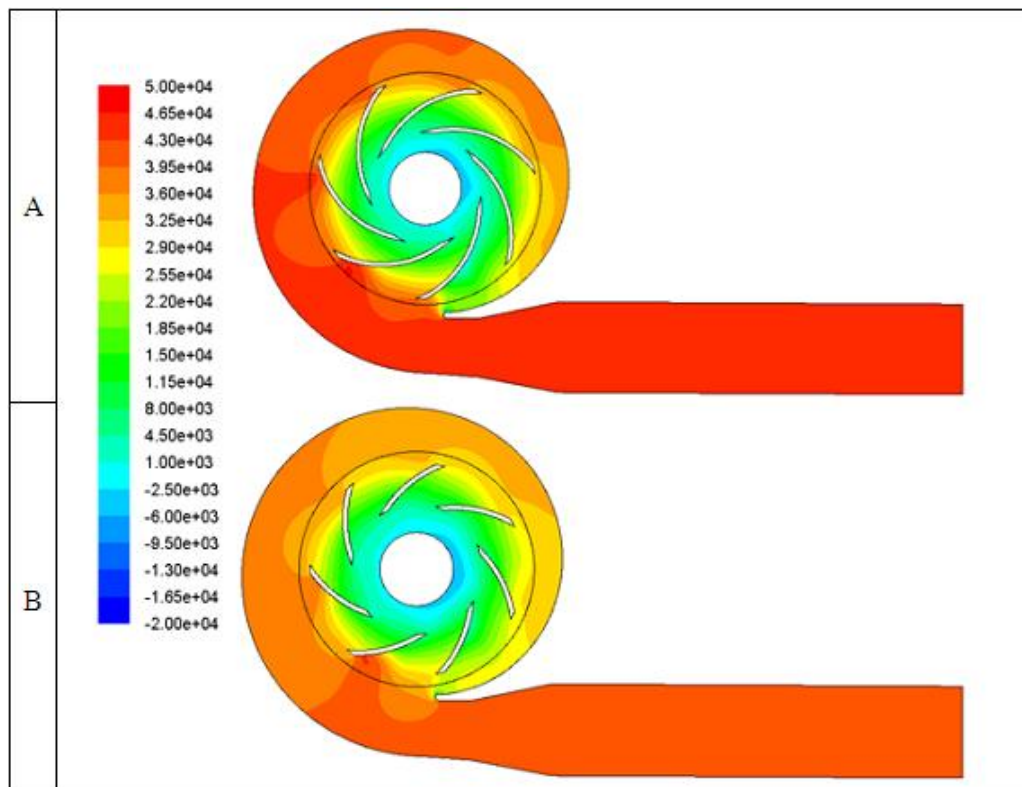
Figure 4.6. Contours of static pressure a. Baseline b. Pareto

Figure 4.7 illustrates the comparison of point pressure variations with time. For a detailed investigation, frequency domain representations were obtained for both pareto and baseline. Since any pressure variation in water can be defined as a sound source, the pressure amplitudes shown in Figure 4.7 can be an indicative for the level of acoustic energy. It is obvious that optimal design contains less acoustic energy.
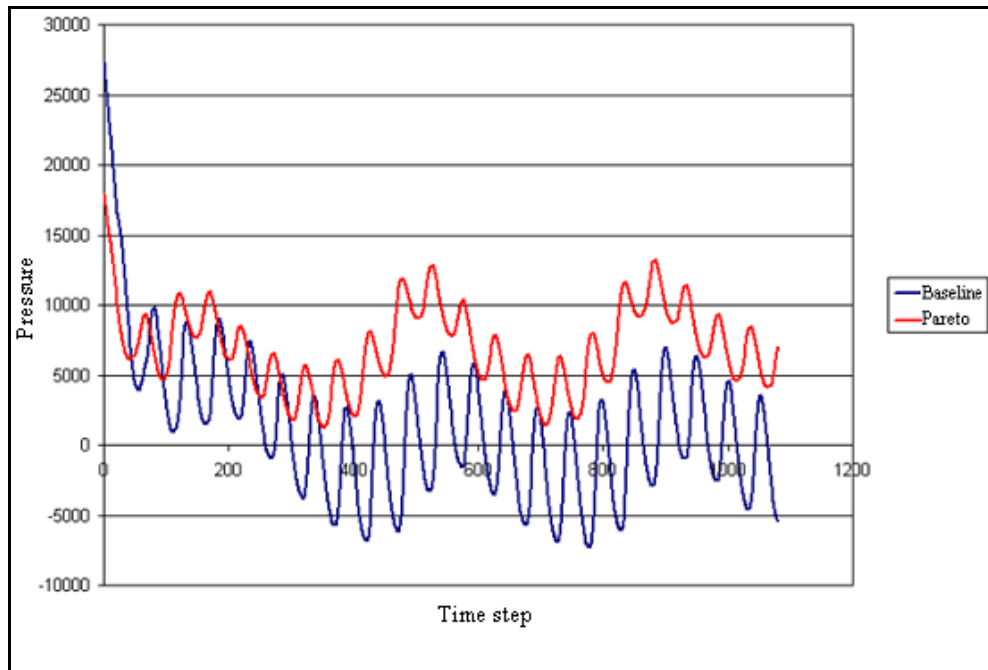
Figure 4.7. Time history of point pressure fluctuations

The influence of geometrical parameters on each response is identified in Table 4.4 where each cell represents correlation between a geometrical parameter and corresponding response. If correlation is zero, it means there is no relationship between the variables. It can be seen that D_2 is the most effective and β_1 is the least effective parameter. A change in β_1 almost does not cause a change in responses. Hence, the geometrical parameter of blade inlet angle β_1 was kept constant in 3-dimensional optimization application.

Table 4.4. Correlation Matrix

variable	impeller vorticity (1/s)	casing vorticity (1/s)	ΔP (Pa)	point_fft_1	point_fft_2
D_1	-0,13008	-0,02171	-0,02132	-0,04243	-0,00025
D_2	0,94797	0,96979	0,99017	0,84475	0,73408
β_1	-0,06207	-0,02118	0,02296	-0,00325	-0,01015
β_2	-0,24670	0,04222	0,10822	0,07586	0,03295

5. 3-D MULTI-OBJECTIVE CENTRIFUGAL FAN OPTIMIZATION

5.1. OPTIMIZATION METHODOLOGY

A simulation-based design optimization method was performed on centrifugal fan. The methodology consists of four stages: (1) determination of design variables and their levels, (2) construction of design matrix using DOE approach and 3-D fan geometry creation, (3) computational grid generation and numerical simulations and (4) evaluation of the results using RSM and identification of optimum configurations.

A built-in Arçelik convection oven is illustrated in Figure 5.1. This type of ovens comprises a blower fan for cooling an electric unit and a centrifugal fan for employing forced air inside the oven. Because the major heat transfer mechanism is forced convection, hot air distribution inside the oven cavity strongly affects the cooking performance especially when cooking more than one item at once. In this study, multi-objective optimization method was performed on a centrifugal fan which is responsible for forced convection as the driving force of cooking.
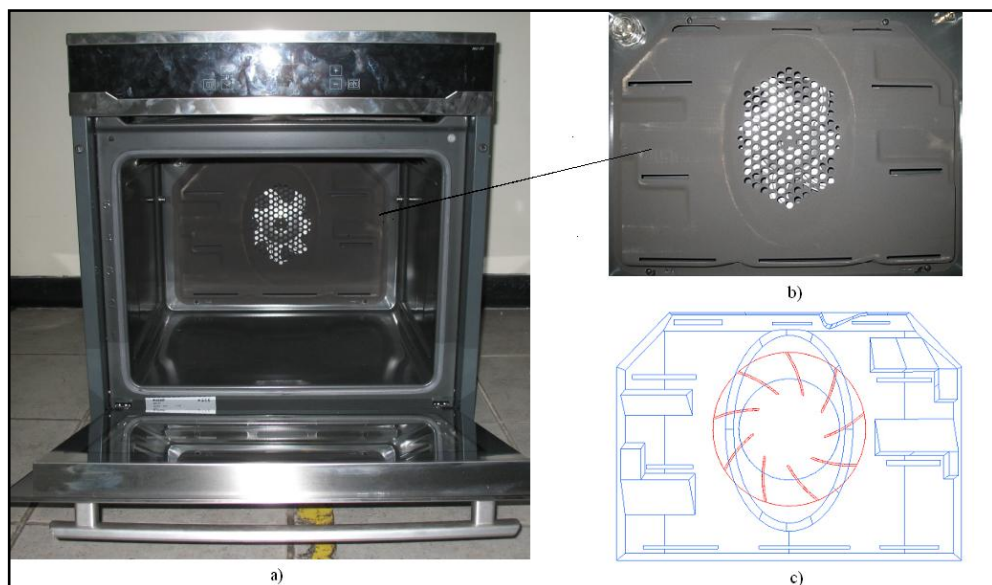
Figure 5.1. a. A built-in convection oven b. The air distribution chamber c. CFD model of the air distribution chamber

The air distribution system consists of a fan and a fan cover. A centrifugal fan is mounted on the rear wall of the box-like cooking chamber wherein food is placed. A fan cover having many small suction holes and 10 blowout ports is fixed to the rear wall to keep the rotating fan out of reach of the users. Air is sucked from cooking chamber through suction holes by the fan. The air temperature is increased when passing through heater element located around fan. The heated air is then distributed into the cooking chamber through blowout ports. The air distribution system except the heater element was embedded in the CFD model (Figure 5.1).

The baseline centrifugal fan consists of backward-curved blades. The number of blades is z. The outer diameter is D_2 and the inner diameter is D_1. The inner tip and hub diameters are $D_{1,tip}$ and $D_{1,hub}$ respectively. The length of the blade is b and the exit angle is β_2. The baseline configuration and physical constraints were considered together when determining the levels of design variables.

In the previous 2-D optimization study, the blade inlet angle was found to be the least effective parameter. Therefore, inlet angle was fixed to be β_1. The blade exit angle, the outer diameter, the number of blades, the blade length, the inner tip diameter and a ratio of inner tip diameter to inner hub diameter were chosen as design variables. These factors are presented in Figure 5.2.
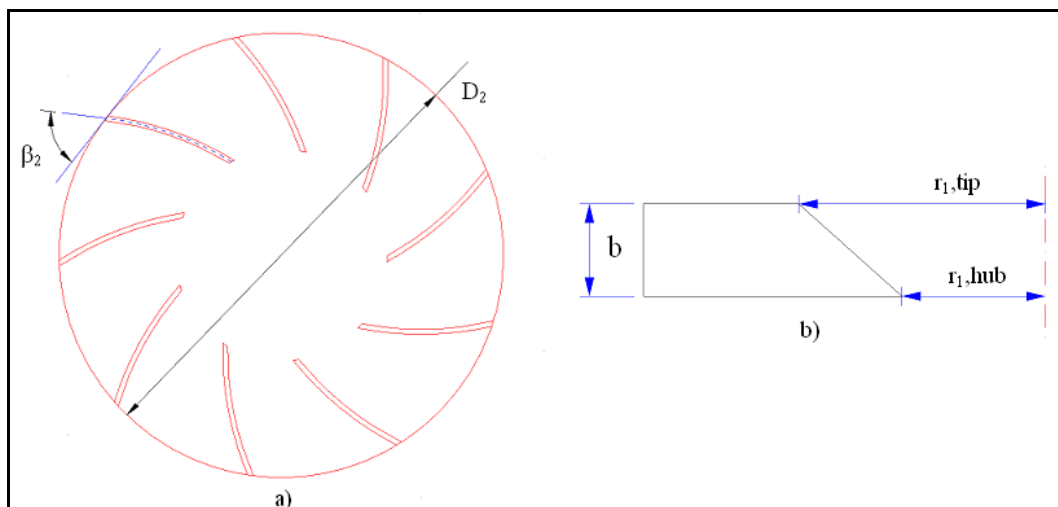
Figure 5.2. The schematic description of design variables a. Impeller top view b. Blade side view

The selection of highest and lowest levels for design variables is a very important issue. The centrifugal fan should be able to operate at these levels. Because of the physical constraints, the outer diameter and the blade length of baseline were adopted as highest levels of related design variables. The levels of blade number were selected on the basis of manufacturing possibility. Therefore, the increment between levels is narrow.

5.1.1. Design of Experiments

In the present study, Minitab software was used to generate the DOE matrix and analyze the response surface model. The 3-level, 6-factor Box-Behnken design was applied to investigate relationship between responses and design parameters. Table 5.1 shows the Box-Behnken design levels used. The factor levels were coded as -1 (low), 0 (central point) and 1 (high).

Table 5.1. Box-Behnken design levels

Parameter	Ranges		
	-1	0	1
outer diameter(mm)	D_2-22	D_2-11	D_2
blade exit angle(°)	β_2-20	β_2-10	β_2
blade length(mm)	b-6	b-3	b
blade number	z-2	Z	z+2
inner tip diameter(mm)	D_1,tip-10	D_1,tip	D_1,tip+10
inner tip diameter/inner hub diameter	1.07	1.17	1.27

The inner tip diameter must be greater than the inner hub diameter for each combination in design matrix. In order to prevent inapplicable runs, a ratio of inner tip diameter to inner hub diameter was selected as a parameter. The DOE matrix including 54 sets of runs with 6 replicates of center point is given in Appendix A.

All 3-dimensional model sketches were obtained using journal files executed by Gambit. Three types of journal files corresponding to three levels of blade number were arranged. They were modified several times for each combination in design matrix. After

3-dimensional models were obtained, fan models were divided into z-2, z or z+2 identical sections depending on blade number in order to implement blocking based approach of structured grid generation.

5.1.2. Computational Grid Generation

Hybrid type computational grids containing both unstructured and structured elements were used in flow simulations. The elements were used according to their properties. Because structured elements are superior near rotating solid boundaries where flow gradients are high, hexahedral elements were utilized around fan blade. Unstructured grid was used to fill the remaining regions where not much is happening in the flow domain.

Unstructured elements were generated in ANSYS ICEM CFD. This mesh generation software uses a blocking-based approach. First a global block was generated around one of identical fan sections. It was then divided into smaller blocks and o-grid block was generated around blade in order to obtain desired grid structure. The grid spacing should be smaller near the solid boundaries and larger when approaching the far field where the flow approaches uniform conditions. Hence, the radial spacing increases from the blade surface to the far field.

The total number of hexahedral elements was nearly equal for each combination in the DOE matrix and thus a risk of mesh dependent results was eliminated.
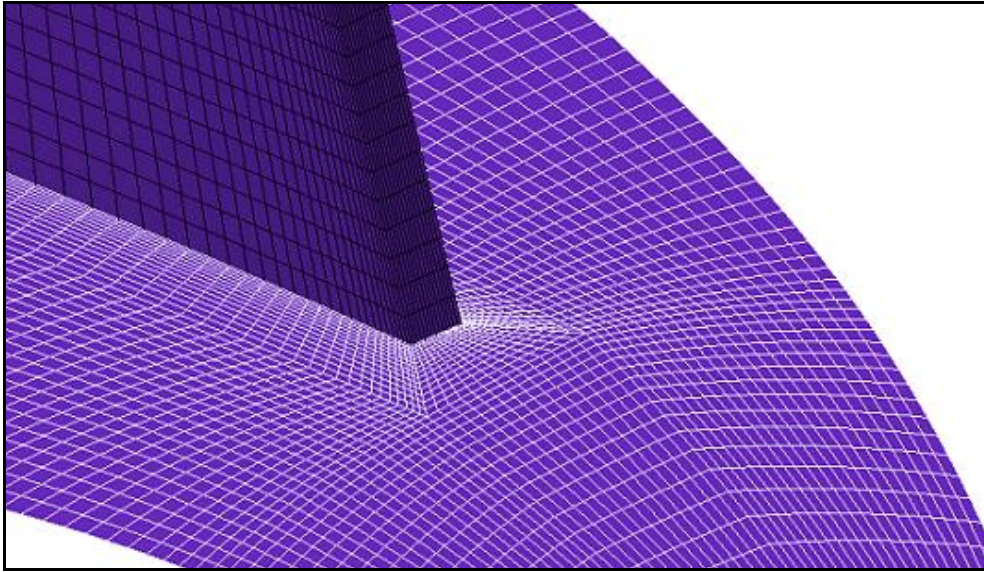
Figure 5.3. The grid distribution near the leading edge of baseline

The generated structured grid on a fan section was rotated by an angle of $(360/z)°$ in order to obtain desired circular fan model. The remaining regions were meshed in Gambit with unstructured elements. A size function was created to reduce the total number of control volumes. The expansion takes place from interface and outlets. The generated final grid contains nearly 2.8 million control volumes.
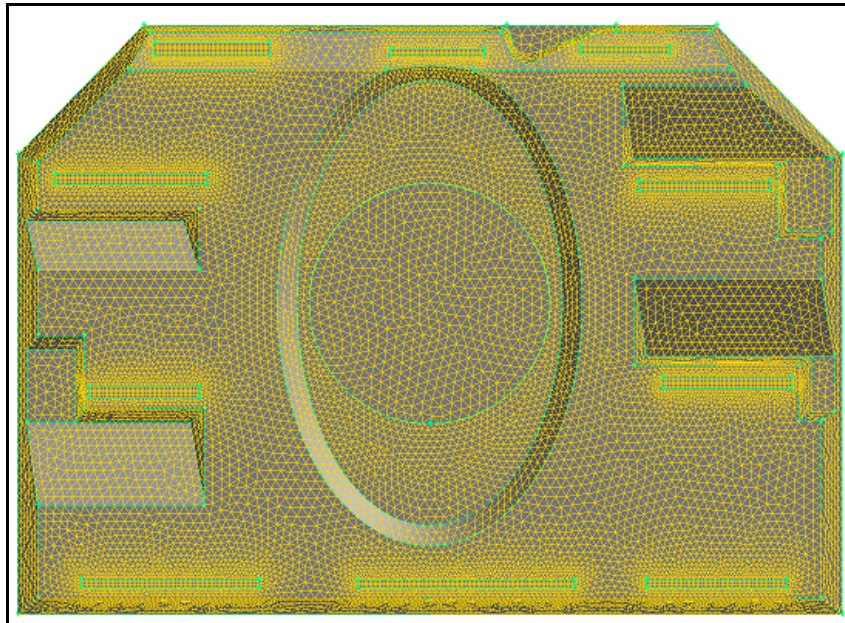
Figure 5.4. The unstructured grid distribution on the fan cover geometry

5.1.3. Validation of Baseline CFD Simulation

The CFD models contain uncertainties due to lack of complete knowledge of the physical processes. The results of flow calculations can differ greatly from one computational approach to another. Hence, comparison of simulation results with measured data is important to validate the model as a basis for optimization.

The meshed geometry of baseline was transferred to the CFD software FLUENT. All necessary boundary conditions were set with taking experimental setup into account for making the experimental and computational boundary conditions same. When the analysis converged to a solution, mass flow rate of each blowout port was recorded. In order to validate CFD results with experiments, mass flow rate measurement was conducted using particle image velocimetry (PIV). PIV method is based on the comparison of two instantaneous images of the same region using seeding particles. These particles are introduced into the flow field and visualized by the help of laser. A camera was used for taking consequent images of flow field. The images were then processed to obtain the velocity distribution on that plane. In comparing the CFD results with experimental data, the experimental errors should be discussed. Several investigations related to the accuracy of PIV evaluations are reported in the literature. It can be stated that PIV method gives fast and accurate results.
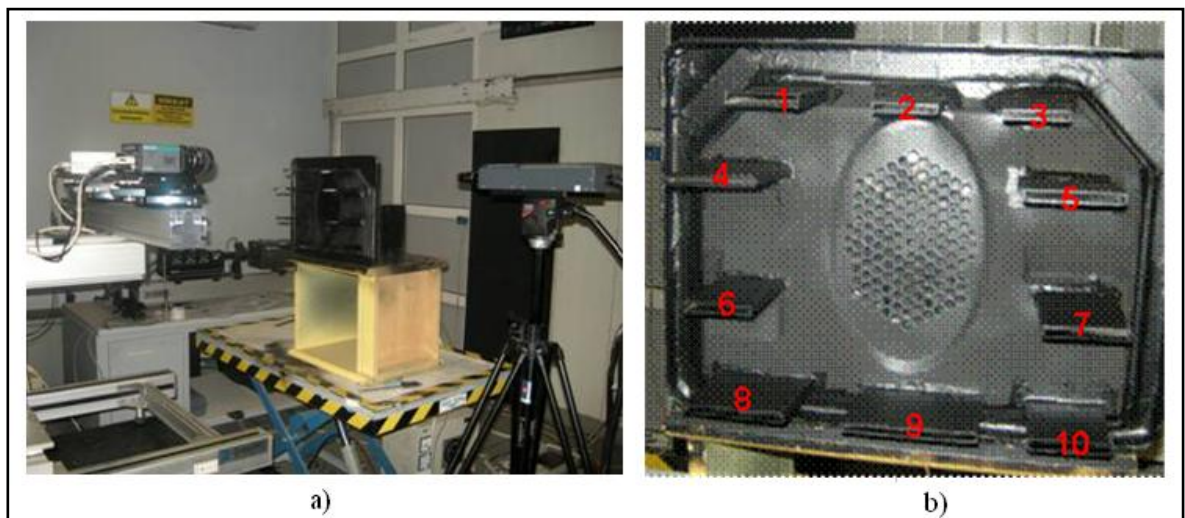
Figure 5.5. a. PIV experimental setup b. The blowout ports

Figure 5.5 shows the experimental setup for the PIV measurement and the enumerated blowout ports. PIV measurements were carried out at Fluid Mechanics Laboratory of Arçelik A.Ş. by technicians. CFD simulation and PIV measurement were both performed under the same circumstances. The fan and cover were separated from oven and fixed to the plate in experimental setup, so that the suction holes and blowout ports became open to the atmosphere. Small geometric simplifications were made in CFD model for mesh generation. These variations do not significantly alter the flow field.

The comparison of the predicted mass flow rate with the experimental value is given in Table 5.2. The mass flow rates from CFD were found to be slightly lower than the PIV measurement except blowout port 5. Results showed that the maximum amount of underestimation is 10.5%. For the total mass flow rate, the disagreement was found to be 7.12%. Kantaş [24] worked on similar model having 6 blowout ports and compared CFD results with Pitot tube air velocity measurements. In his study, disagreements ranging from 13.79% to 16.67% were observed. The CFD results can be said to be in reasonably good agreement with the experimental PIV data. The overall good agreement between PIV and CFD suggests that CFD can reliably predict the optimization responses.

Table 5.2. The comparison of predicted and measured mass flow rate

	Mass Flow Rate (l/s)		
Blowout Port	PIV	CFD	Disagreement (%)
1	1,83	1,64	10,26
2	0,6	0,55	8,16
3	0,5	0,47	6,89
4	1,61	1,57	2,61
5	1,23	1,24	-1,12
6	1,21	1,10	8,55
7	1,72	1,56	9,53
8	1,48	1,36	8,35
9	1,43	1,28	10,50
10	1,16	1,09	5,91
Total	12,76	11,86	7,12

5.1.4. Flow Simulations

Flow field calculations were carried out by Fluent. By the help of a CFD solution of the baseline fan that was validated against PIV data, all necessary boundary conditions, turbulence model and other CFD subroutines were defined. The effects of turbulence were modeled using the standard k-ε model with standard wall functions. The boundary conditions were set according to the experimental setup. The air suction holes, which were modeled with a single circular face, were assumed to be pressure inlet type while blowout ports were assumed to be pressure outlet type in all configurations. The rotational speed of fans was set to 960 rpm.

Fluent has both steady and unsteady solver options. The unsteady solver is used for dynamic simulations where you are integrating in time and consumes substantial amount of computational effort for optimization purpose. In this study, the flow field was assumed to be steady with constant boundary conditions and governing equations were solved in segregated solver.

The discretization of viscous terms is second order in Fluent but the order of discretization for convective terms in the equations can be set by the user. The default discretization parameter of first order upwind was adopted for momentum, turbulent kinetic energy, and turbulent dissipation rate. Standard discretization was set for pressure. Pressure-velocity coupling was achieved by the SIMPLE scheme. The under relaxation factors of 0.3 for pressure, 0.5 for momentum, 0.6 for both k and ε were used.

All combinations in the doe matrix were analyzed and the results acquiring a different character are illustrated in figures. Figures 5.6 to 5.13 are the Fluent outputs providing details of the flow characteristics.
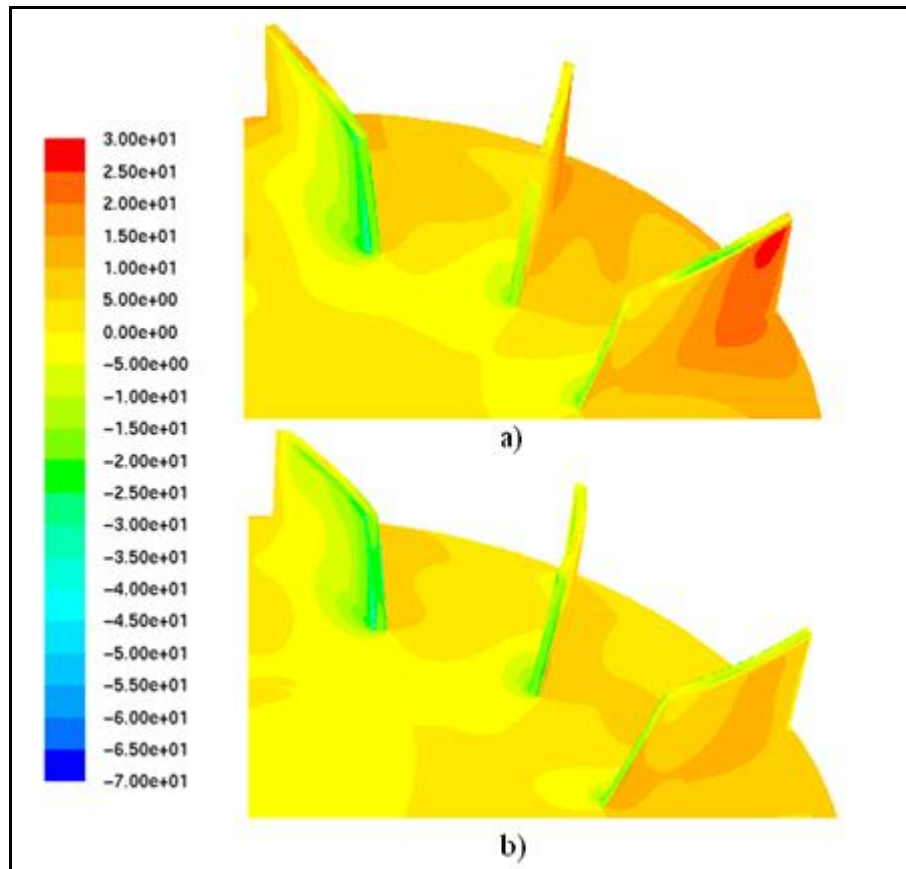
Figure 5.6. Contours of pressure on the blade surfaces a. Fan # 23 b. Fan # 4

Figure 5.6 shows contours of surface pressure on the discharge and suction side of the fan blades. On the suction side pressure is low around inlet portion and then gradually increases. No significant difference seems to exist for suction pressures of all simulated fans. On the other hand, characteristics of discharge pressure considerably vary from fan to fan. The surface pressure distribution has its maximum value at the tip of the trailing edge of fan # 23. Fan # 4 has less desirable distribution. Pressure slightly decreases at the trailing edge.

The static pressure distributions on an axial slice passing through the mid-plane of the fan blade are shown in Figure 5.7. The pressure distribution illustrates sudden pressure variation regions where the flow begins to circulate. These regions are formed in both models because of the complex geometry of a fan cover which acts as an air guide. The aerodynamic performance of a centrifugal fan can be specified in terms of its pressure rise

characteristic. The difference in pressure rise through the fan is clearly seen in Figure 5.7. Compared to centrifugal fan # 21, fan # 14 appears to provide much better performance.
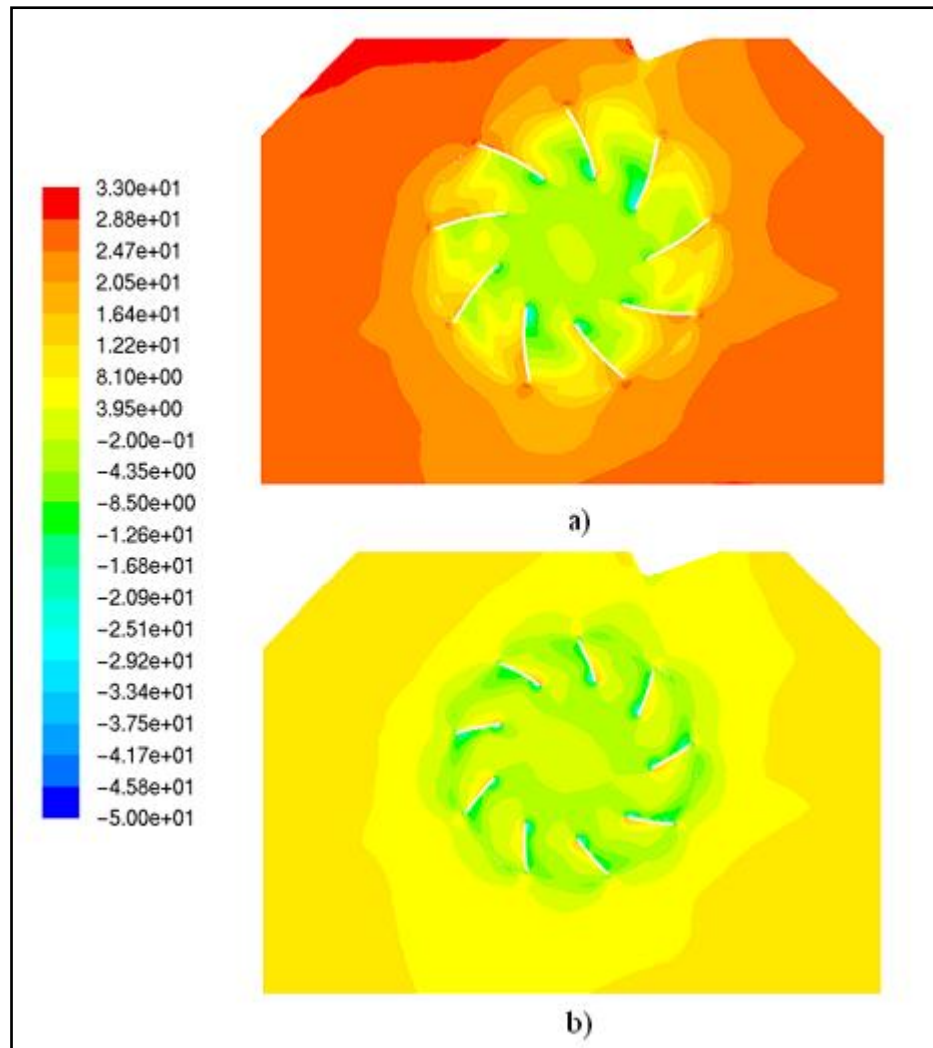
Figure 5.7. Contours of pressure on the mid-plane a. Fan # 14 b. Fan # 21

Figures 5.8 and 5.9 illustrate relative velocity vectors representing the details of the flow field inside a fan section. Although a localized recirculation zones were predicted at the leading edge, the air shows a regular flow pattern between blades in all configurations. Conserving a regular flow pattern in this region, that is an important performance trend, improves the efficiency of the fan. The vector plots show that the flow is fairly smooth.
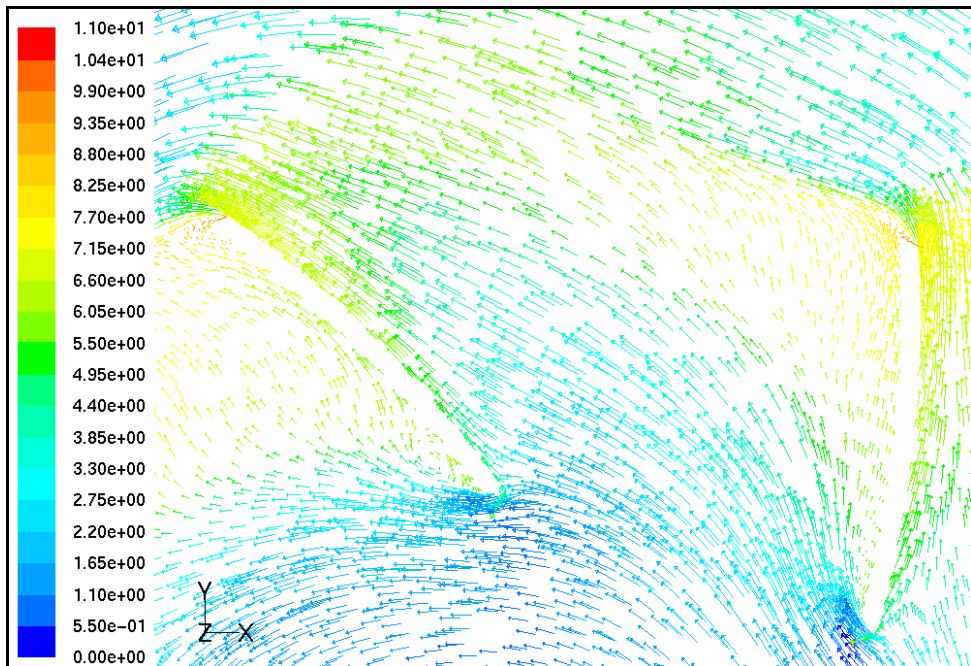
Figure 5.8. Relative velocity vectors between the fan blades (Fan # 15)
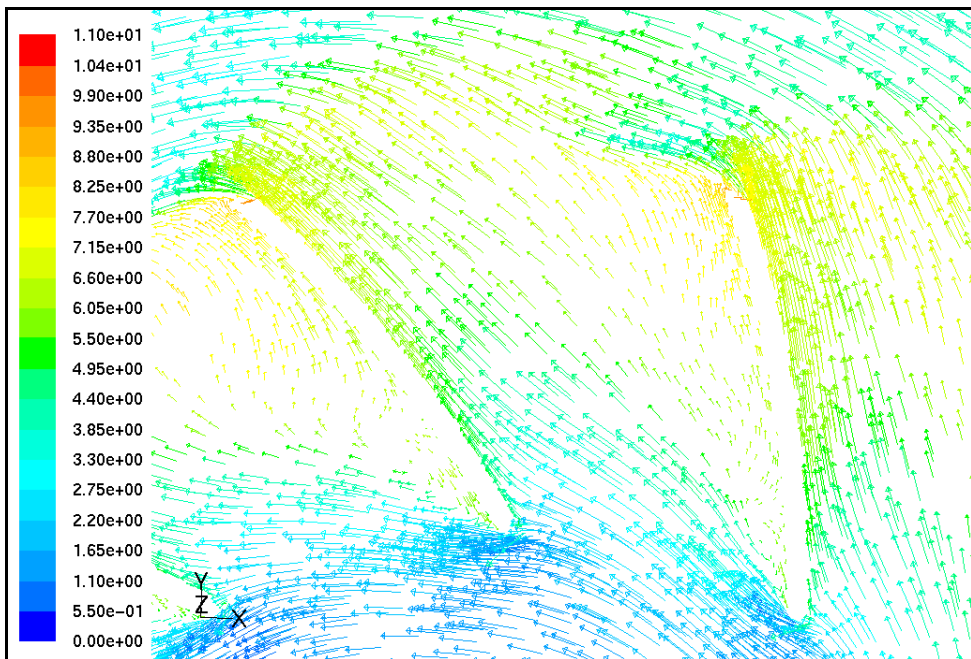
Figure 5.9. Relative velocity vectors between the fan blades (Fan # 40)

The vector plots of velocity magnitude on a plane perpendicular to the plane of rotation are displayed in Figures 5.10 and 5.11 in order to investigate the effects of a gap at

the blade tip. Due to the pressure difference between two sides of the blade, flow leaks into the fan inlet through the tip gap and mix with the main flow. This leakage flow causes a decrease in the efficiency of the fan, and thus it should be minimized.
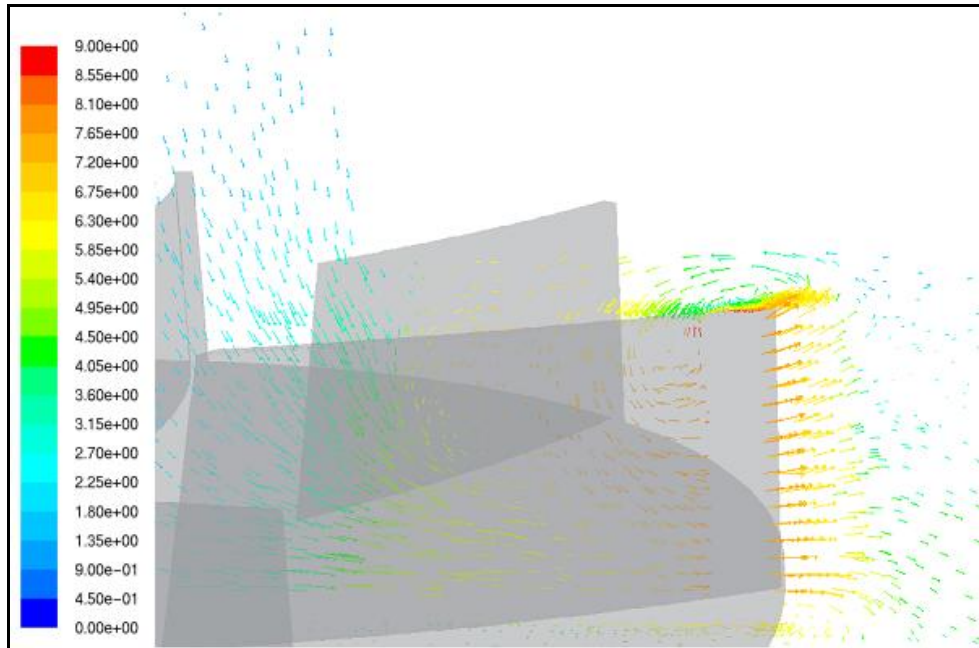
Figure 5.10. Velocity vectors at the blade tip (Fan # 49)
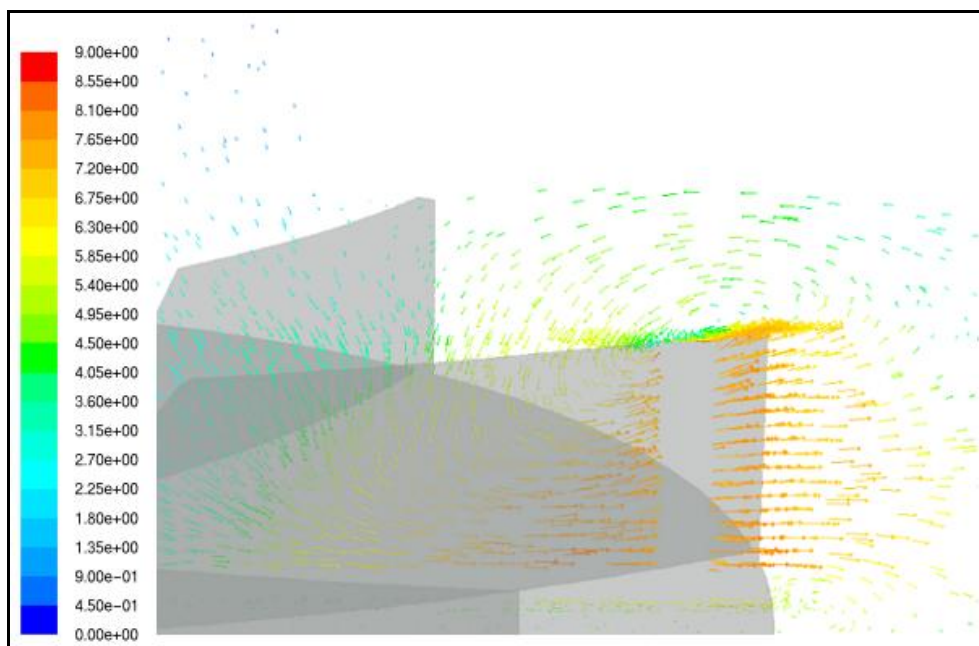
Figure 5.11. Velocity vectors at the blade tip (Fan # 50)

Since the tip gap of fan # 50 is 6 mm broader than that of fan # 49, a significant amount of leakage flow into the suction side is observed in Figure 5.11. Total pressure losses are directly proportional with the tip gap distance. When the tip gap is large, the pressure difference between the pressure side and the suction side starts to decrease and as a result fan performance is deteriorated. It is obvious that the efficiency of fan # 50 is lower than the efficiency of fan # 49 due to tip gap related losses.

Figures 5.12 and 5.13 show contours of vorticity magnitude that indicate regions where the disturbances are high. The theory of vortex sound suggests that higher vorticity indicates strong disturbance in the flow and hence higher aerodynamic noise level which accounts for most of the noise in centrifugal fans. Therefore, the scale and intensity of vortex structures can be compared in order to examine aeroacoustic performance.
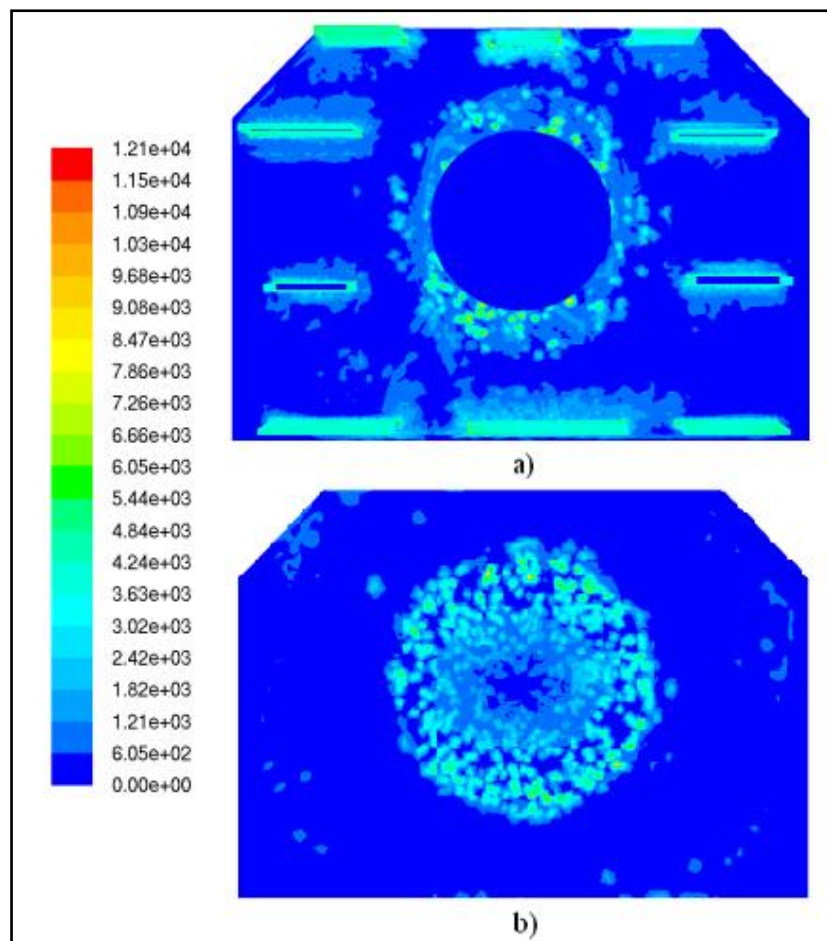
Figure 5.12. Contours of vorticity magnitude (Fan # 27, casing) a. Front b. Back view

Because an identical casing configuration was used in all numerical simulations, contours of vorticity magnitude are displayed on casing surfaces. In Figure 5.13 it can be seen that the vortex structures of fan # 21 are rarely seen and their scales are smaller. On the contrary, for fan # 27 as shown in Figure 5.12, the disturbance zones in which noise generation is concentrated are stronger and more intense in the flow field. It can be concluded that the aeroacoustic performance of fan #21 is better than that of fan # 27.
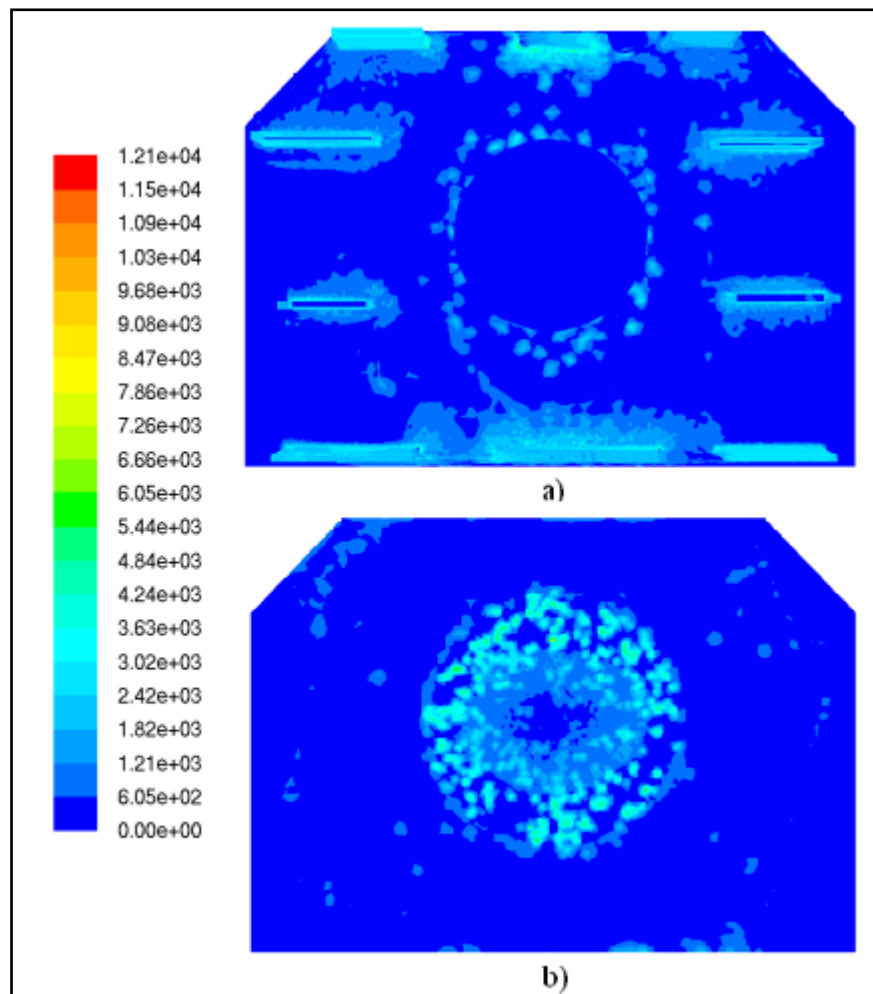
Figure 5.13. Contours of vorticity magnitude (Fan # 21, casing) a. Front b. Back view

5.1.5. Response Surface Analysis

Response surface methodology (RSM) aims to replace the complex responses of the processes by simple implementing polynomials. The first goal of RSM is to find the region

where the optimal response occurs. Since the relationships between three different responses and the set of independent variables are investigated in this study, it is important to find the optimum that optimizes all responses and meet needs of the constraints. The construction of RSM is based on the use of the numerical simulations with six design parameters. In RSM technique, an appropriate order polynomial is fitted to a set of numerically evaluated data points, and then a response surface is created between design variables and objective functions. Numerical response data on noise generation (area-weighted average vorticity magnitude and standard deviation of pressure on casing surfaces) and aerodynamic performance (mass flow rate) were obtained for each of the configurations identified by the DOE. The table of these predicted responses and the correlation matrix that represents the influence of design variables on responses is given in Appendix A. The analysis of results was performed with Minitab software.

The response surface can be visualized graphically in order to understand how the response changes according to design variables. In the surface plot, response surface is represented as a solid surface in a three-dimensional space. In the contour plot, lines of constant response are drawn and hence pairs that have the same response value can be identified. When there are more than two independent variables, it is impossible to display response surface graphically. For this reason, two variables were selected for a response and corresponding response surfaces are illustrated in surface and contour plots. Since there are six design variables, each time four factors were hold at a constant level when plotting the other two variables. The response surface changes depending on holding levels. The high settings are selected as holding levels for the other factors in all contour and surface plots.
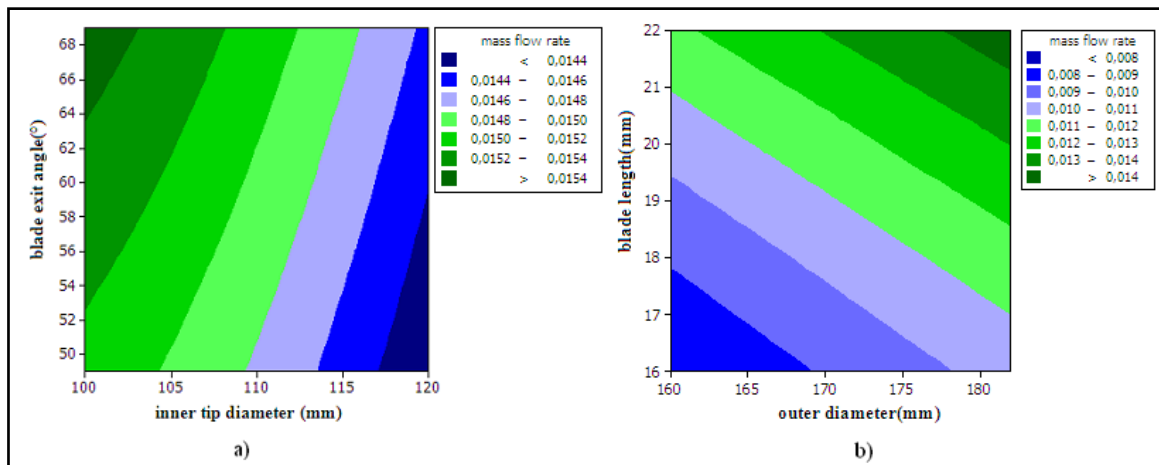
Figure 5.14. The contour plots of mass flow rate a. blade exit angle vs inner tip diameter b. outer diameter vs blade length
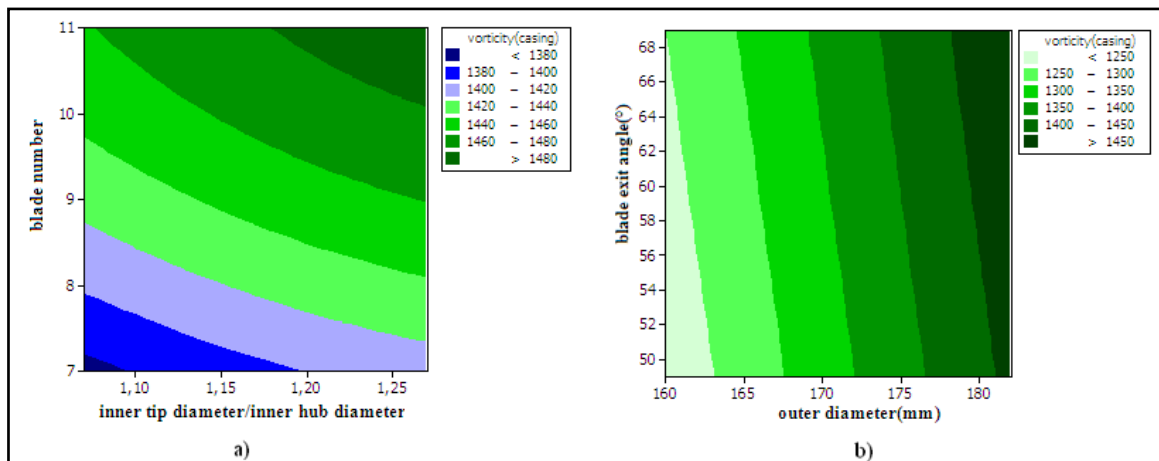
Figure 5.15. The contour plots of area-weighted average vorticity on casing a. blade number vs ratio of inner diameters b. outer diameter vs blade exit angle

Figure 5.14 and 5.15 show the contour plots of mass flow rate and area-weighted average vorticity on casing. These plots indicate how mass flow rate and vorticity relate to the two factors. Each contour corresponds to a particular height of the shape of the response surface. The response is at its highest value at the dark green region.
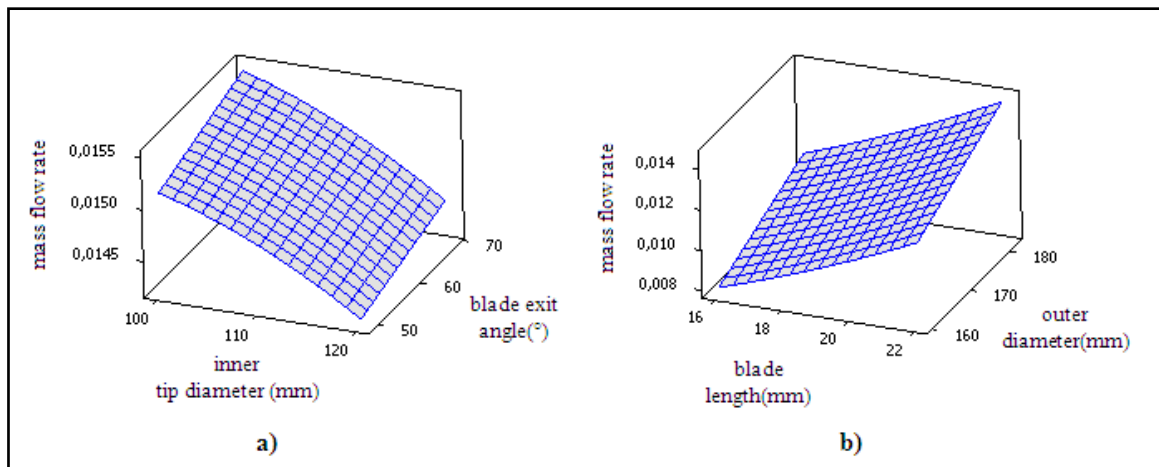
Figure 5.16. The response surface plots of mass flow rate a. blade exit angle vs inner tip diameter b. outer diameter vs blade length

Response surface plots of responses (mass flow rate and standard deviation of pressure on casing) as a function of two factors at a time are shown in Figures 5.16 and 5.17. These figures illustrate mutual effect of two design variables on responses, while other four variables are maintained at high level. From the response surface plots in Figure 5.16 it can be seen that a variation in blade exit angle and inner tip diameter causes a relatively less change in response. Mass flow rate is predominantly influenced by blade length and outer diameter. Figure 5.17 indicates that ratio of inner diameters almost does not effect the response. The response of standard deviation of pressure on casing decreases when moving from the high level to the low level for blade number, and blade exit angle and from the low level to the high level for inner tip diameter.
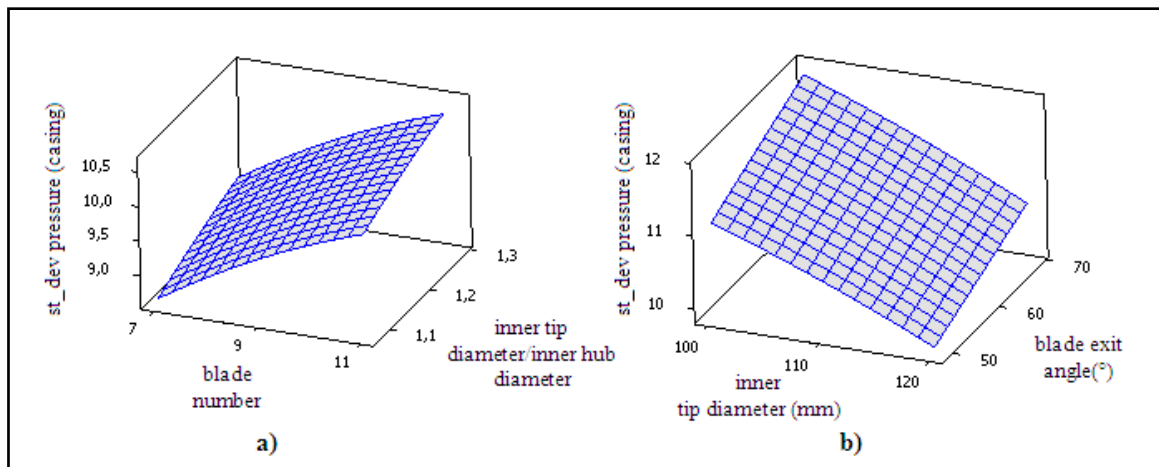
Figure 5.17. The response surface plots of standard deviation of pressure on casing a. blade number vs ratio of inner diameters b. blade exit angle vs inner tip diameter

5.1.6. Pareto Designs

The Minitab's Response Optimizer application was used to identify the combination of design variables that jointly optimize a combination of responses. Optimal settings of the design variables for one response may be far from optimal for another response. Response optimizer provides suggestions for variables based on the results of the RSM and allows for compromise among the various responses. The various optimal solutions can be obtained by a choice of the weight, the upper and lower values of each variable. For each response, a weight can be selected from 0.1-10 to highlight the importance of the target.

In order to perform response optimization, the goals for each response were determined. For mass flow rate, the goal was determined to be its maximization since it is an aerodynamic performance indicator and desired to be as high as possible. The goal for the vorticity and standard deviation of pressure on casing surfaces were to be kept at minimum values. The upper and lower values were determined according to the simulation of baseline configuration. Because most effective design variables of outer diameter and blade length were at highest level for baseline, no optimal solution having better aerodynamic and aeroacoustic performance was found. For this reason, the maximum reduction of 14% in mass flow rate was considered as acceptable. A weight value of 1

which emphasizes equivalent importance was selected for each response. The optimal solutions were obtained for two different conditions. In Table 5.3, the detailed description of evaluation criteria is given.

Table 5.3. Evaluation criteria description for response optimizer

Pareto 1					
Response	Goal	Lower	Target	Upper	Weight
mass flow rate (kg/s)	Maximize	0.0125	0.0129		1
vorticity (casing) (1/s)	Minimize		1310	1400	1
St_dev pressure (casing) (Pa)	Minimize		8.2	9.5	1
Pareto 2					
Response	Goal	Lower	Target	Upper	Weight
mass flow rate (kg/s)	Maximize	0.0133	0.0136		1
vorticity (casing) (1/s)	Minimize		1380	1450	1
St_dev pressure (casing) (Pa)	Minimize		8.8	9.5	1

The optimal configurations were analyzed using the same numerical procedure. The fitting quality of the response surface model indicates the usefulness of the optimization methodology. If the fitted surface is an adequate approximation, the analysis of the fitted surface represents the analysis of the actual system. Table 5.4 shows the comparison of the response surface model results and the CFD results. The difference is small for all responses. This result verifies that the fitted model provides an adequate approximation to the actual system.

Table 5.4. Comparison of RSM and CFD results

	mass flow rate (kg/s)		vorticity (casing) (1/s)		st_dev pressure (casing) (Pa)	
	RSM	CFD	RSM	CFD	RSM	CFD
Pareto 1	0.0129	0.0128	1315.3	1298.8	8.2	8.12
Pareto 2	0.0136	0.0135	1382.6	1375.8	8.99	8.97

5.2. COMPARISON OF OPTIMAL DESIGNS WITH BASELINE

According to CFD results (Table 5.5), the optimal configurations present 11.8% and 7% less mass flow rate in comparison to baseline. This reduction is conceivable because mass flow rate is greater than the allowable minimum value. The optimal designs can still provide adequate aerodynamic performance. Area-weighted average vorticity magnitude and standard deviation of pressure on casing surfaces are numerical response data related to noise generation and hence desired to be kept as low as possible. The optimal designs present a notable reduction of these noise level determining responses. Pareto 1 and Pareto 2 exhibit vorticity reduction of 13% and 8%, respectively. The standard deviation of pressure response is 23% lower for Pareto 1 and 15% lower for Pareto 2 than that of baseline configuration. It can be stated that the optimal designs contain less acoustic energy.

Table 5.5. Comparison of baseline and optimal designs (CFD results)

	mass flow rate (kg/s)	vorticity (casing) (1/s)	st_dev pressure (casing) (Pa)
Baseline	0,0145	1495,79	10,57
Pareto 1	0,0128	1298,80	8,12
Pareto 2	0,0135	1375,77	8,97

The improvement in vorticity can be seen clearly in Figure 5.18. This figure illustrates the regions on casing surfaces where disturbances are high. The disturbance zones are stronger and dense at locations close to rotating centrifugal impeller in all configurations. Since higher vorticity indicates strong disturbance in the flow, the scale and intensity of vortex structures can be used to determine relative aeroacoustic performance. In comparison to baseline and Pareto 2, the vortex structures of Pareto 1 are seldom seen on casing surfaces and their scales are smaller. According to comparison of the scale and intensity of disturbance regions, the noise level of Pareto 1 is lower with respect to baseline and Pareto 2. The noise level of Pareto 2 is between that of Pareto 1 and baseline. In terms of aeroacoustic performance, baseline is the worst fan.
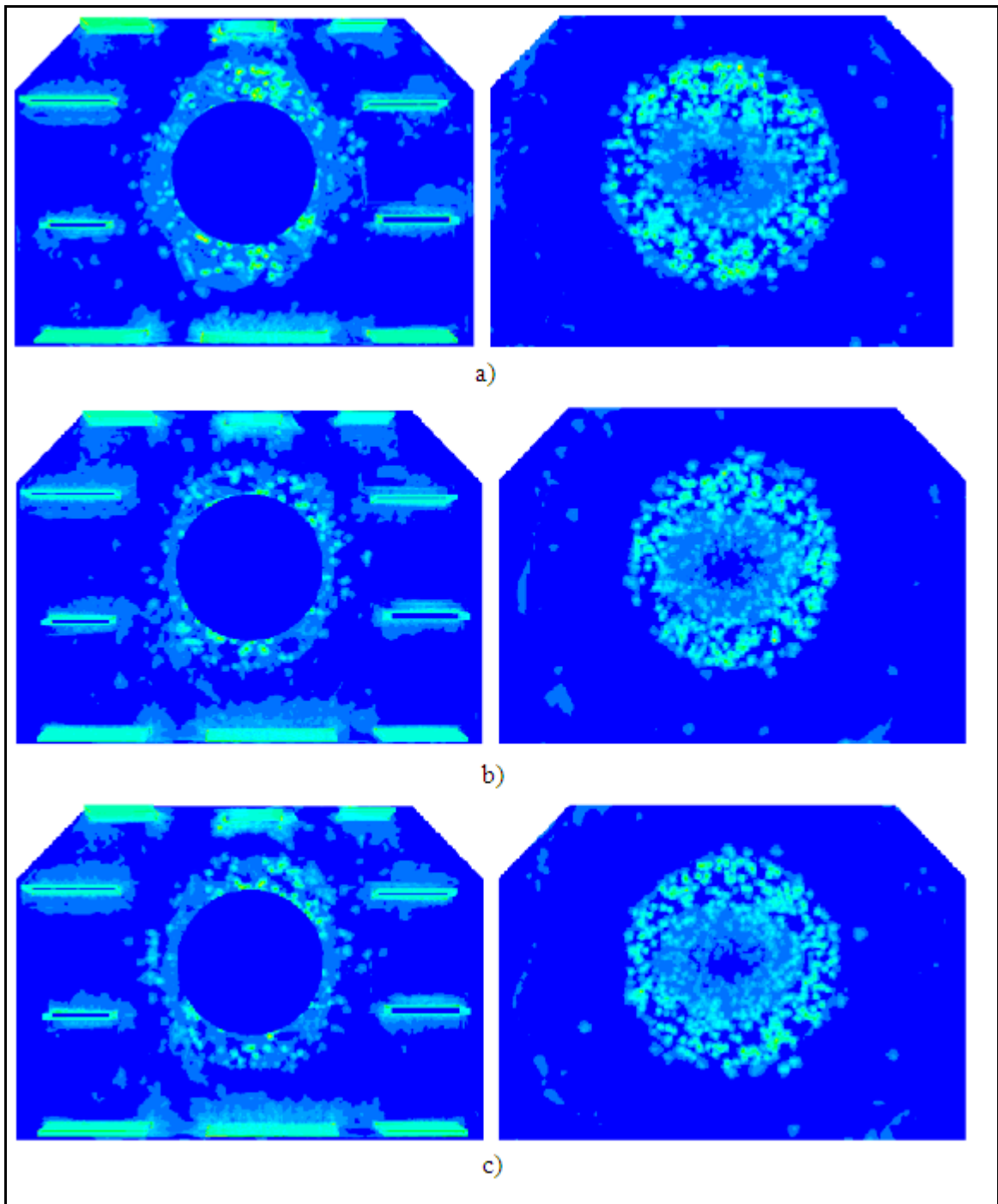
Figure 5.18. Contours of vorticity magnitude on casing surfaces a. Baseline b. Pareto 1 c.
Pareto 2

It is known that noise generation mechanism is linked to the existence of vortical
structures. For a better understanding of this relationship and for testing the effectiveness

of optimization methodology, the prototypes of optimal designs were produced and noise measurements were performed.

5.2.1. Noise Measurements

An experimental approach was adopted to measure noise level directly. The measurements were conducted in a semi-anechoic test room of Arçelik A.Ş. Vibration and Acoustics Laboratory using prototypes of baseline and optimal designs. Figure 5.19 shows the set-up and microphone positions. To ensure a reliable outcome for evaluation, noise measurements were performed using the same set-up as in PIV experiments.

Figure 5.19. Experimental set-up

Noise of the centrifugal fan was determined with a series of experiments for four different fan speeds in order to show the influence of the rotational speed on the noise generation. Table 5.6 shows the overall A weighted sound power level ($L_w(A)$) for all the configurations measured. It is observed clearly that L_w tends to increase if the rotational speed increases.

Table 5.6. Overall A-weighted L_w of baseline and optimal designs

Rotational Speed (rpm)	L_w (dBA)		
	Baseline	Pareto 1	Pareto 2
960	54.3	51	52
1020	55.9	53	53.7
1080	57.5	53.8	55.5
1140	58.9	54.9	57.5

The optimal configurations present a considerable reduction of noise level at the entire fan rotational speed range. The overall noise levels are 54.3, 51, 52 dBA at 960 rpm for baseline, Pareto 1 and Pareto 2, respectively. Pareto 1 exhibits L_w reduction of 3.3 dBA in comparison to baseline. The noise level obtained at 960 rpm for Pareto 2 is 2.3 dBA lower than the corresponding level of baseline. The observed trends are similar at 1020, 1080 and 1140 rpm. According to the experimental results, Pareto 1 has better advancement of noise reduction at all different fan speeds. The overall A-weighted L_w of Pareto 2 is between those of Pareto 1 and baseline at the whole fan rotational speed range.

In Figures 5.20, 5.21, 5.22 and 5.23, one-third octave band frequency L_w spectra at 960, 1020, 1080 and 1140 rpm for baseline and optimal designs are presented. The frequency range is divided into bands, for which time-averaged values are obtained. Each band covers a specific range of frequencies and except all others. Although higher levels are present at frequencies lower than 100 Hz, optimal configurations present notable reduction at the medium and high frequency range with respect to baseline. The measured sound power is highly dependent on frequency. The improvement of sound power is especially important in the range of frequencies between 1000 and 2000 Hz where the human ear is very sensitive. It is observed that the contributions at these frequencies are not present as high peaks but extend over frequency range.

Figure 5.20. 1/3 octave band frequency sound level spectra (960 rpm)
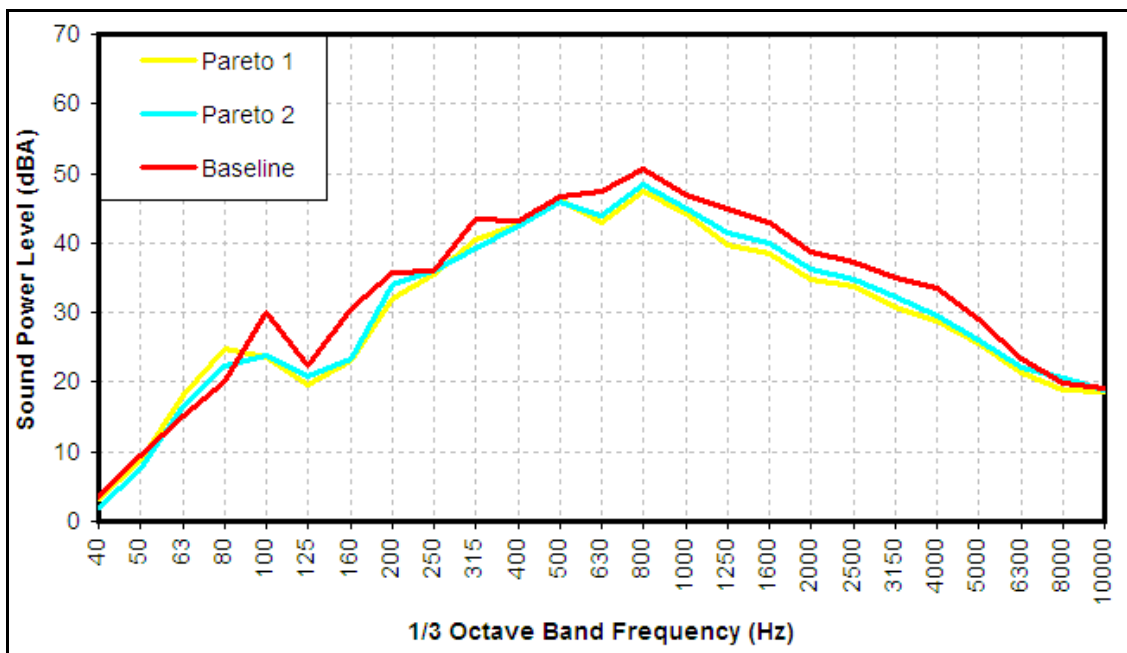
Figure 5.21. 1/3 octave band frequency sound level spectra (1020 rpm)

In all L_w spectra, Pareto 1 and Pareto 2 exhibit relatively low noise level over wide frequency bands. Figures of L_w suggest that dominant mode occurs at the one-third octave

band of 800 Hz. The excitation of baseline at this frequency is higher at all fan speeds in comparison to Pareto 1 and Pareto 2 as shown in Figures 5.20, 5.21, 5.22 and 5.23.
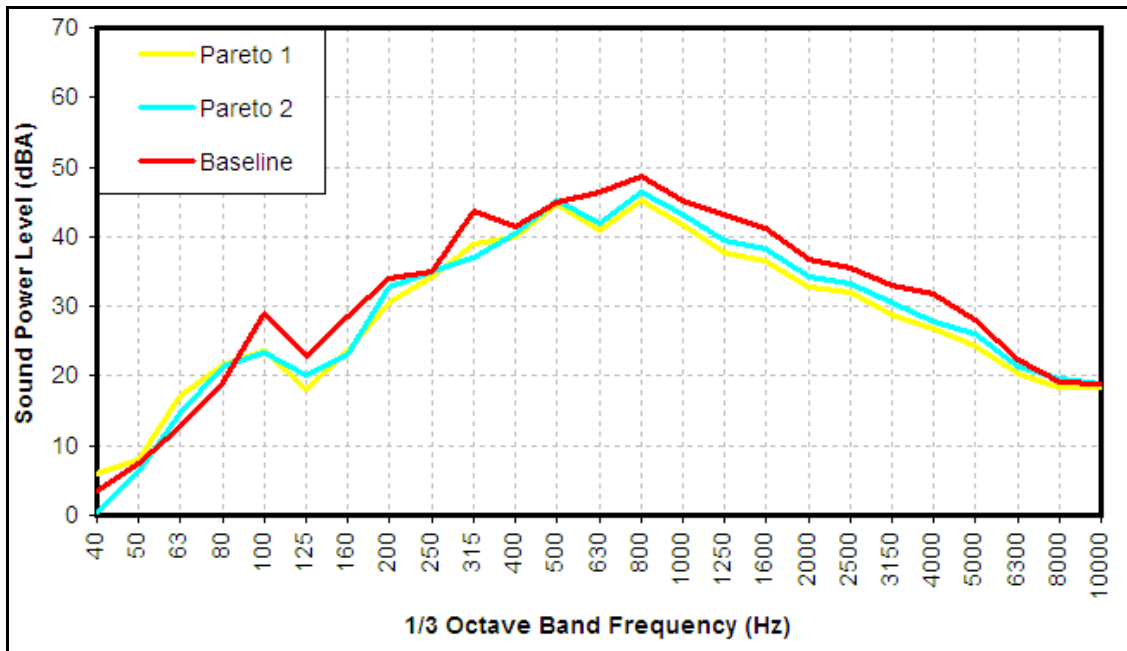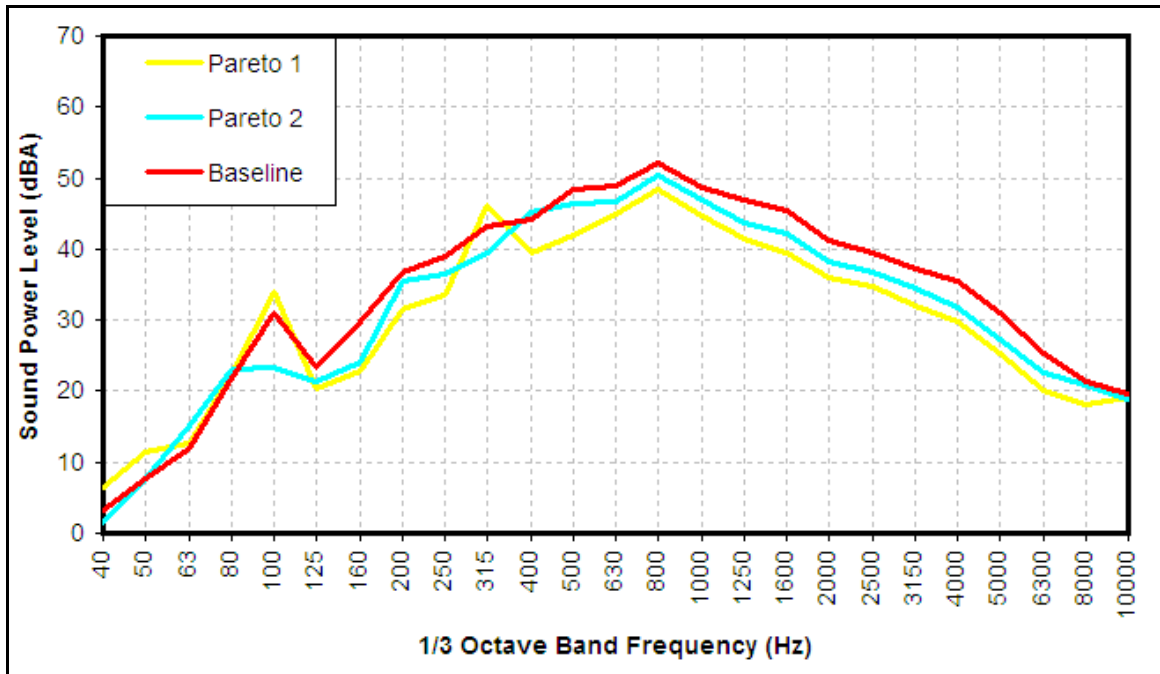

Figure 5.22. 1/3 octave band frequency sound level spectra (1080 rpm)
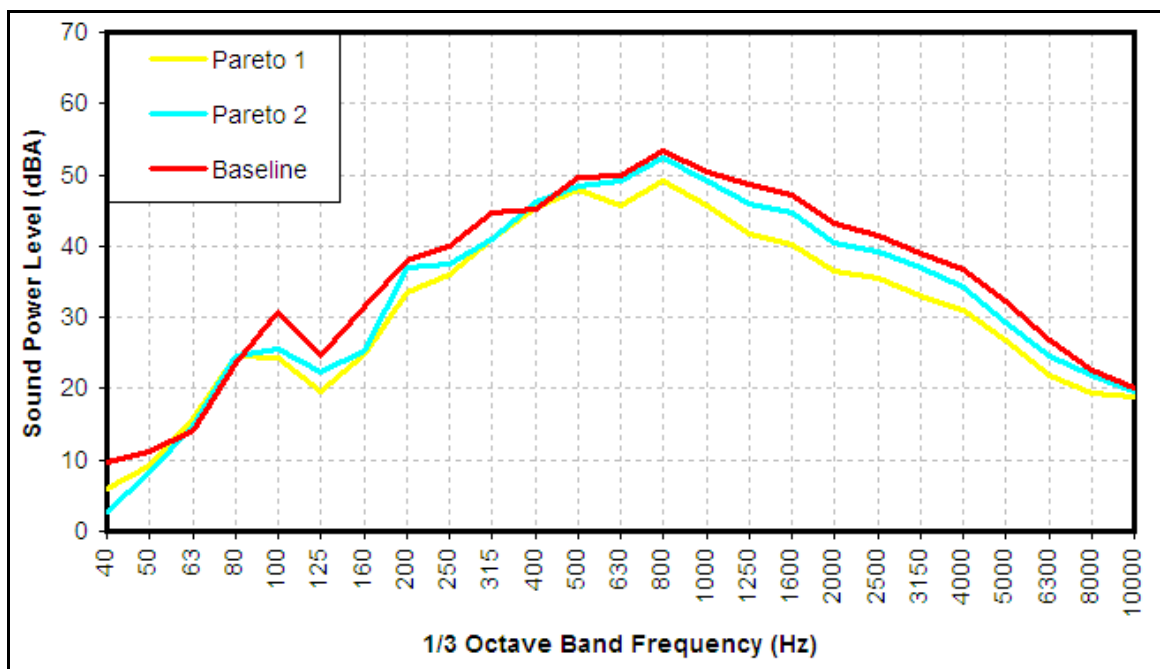
Figure 5.23. 1/3 octave band frequency sound level spectra (1140 rpm)

6. CONCLUSION

A simulation-based optimization method was developed and applied to the aerodynamic and aeroacoustic optimization of centrifugal type convection oven fan. The optimization method uses design of experiments (DOE) based response surface methodology (RSM). The shape of centrifugal fan was parameterized by six design variables and hence Box-Behnken design matrix was constructed for six factors. All combinations in this matrix were simulated.

Flow field calculations were carried out by Fluent with hybrid type computational grids containing 2.8 million unstructured and structured elements. The effects of turbulence were modeled using the standard k-ε model with standard wall functions. The flow field was assumed to be steady with constant boundary conditions. The air suction holes were assumed to be pressure inlet type and blowout ports were assumed to be pressure outlet type boundaries. The rotational speed was set to 960 rpm.

In order to validate CFD results, mass flow rate measurement for baseline configuration was conducted using PIV. The comparison of the predicted mass flow rate with the experimental data shows that the CFD results are in good agreement with the PIV data (maximum 10.5% underestimation). The good agreement demonstrates that CFD can accurately predict the optimization responses and can be used as a basis for optimization.

The influences of design variables on responses were investigated and identified in terms of correlation value. It was determined that outer diameter and blade length are the most effective design variables with a correlation value greater than 0.5 for all responses. In contrast, a ratio of hub diameters and blade inlet angle are the least effective design parameters of centrifugal turbomachinery configurations in terms of aerodynamic and aeroacoustic performance. A variation in these parameters does not cause a remarkable change in responses.

RSM was employed in order to find the optimal solution that optimizes all responses and meet requirements of objectives using a set of numerically predicted response data.

The optimal solutions were obtained for two different evaluation criteria. The optimal configurations were analyzed using the same numerical procedure. The difference between the response surface model results and the CFD results is very small. This result proves that the fitted surface is a reliable representation of the actual system.

Because of the physical constraints, the most effective parameters of outer diameter and blade length of baseline were adopted as high design level instead of central design level. Therefore, no solution having same aerodynamic performance with baseline and lower noise level was found in a defined domain. Oven can still provide adequate cooking performance with the maximum reduction of 14% in mass flow rate. The optimal solutions (Pareto 1 and Pareto 2) were obtained for this reduction limit of aerodynamic performance. According to the CFD results, the optimal configurations present 11.8% and 7% less mass flow rate in comparison to baseline. Pareto 1 and Pareto 2 exhibit notable vorticity reduction of 13% and 8% with respect to baseline. In addition, the standard deviation of pressure response is 23% lower for Pareto 1 and 15% lower for Pareto 2 than that of baseline.

According to improvements in noise generation related responses, it can be said that optimal designs contain relatively less acoustic energy. In order to identify exact influence of improvements on noise generation, the prototypes of optimal designs were produced and noise measurements were experimentally performed. It is observed that Pareto 1 exhibits L_w reduction of 3.3 dBA in comparison to baseline at 960 rpm (defined rotational speed in CFD). The noise level measured at 960 rpm for Pareto 2 is 2.3 dBA lower than that of baseline. Noise level of the centrifugal fan was measured for four different fan rotational speeds. The optimal configurations present a considerable reduction at all fan speeds. Pareto 1 configuration shows the best improvement in responses of vorticity and standard deviation of pressure on casing surfaces, has the lowest noise level and hence the best aeroacoustic performance as expected. Pareto 2 is between in baseline and Pareto1 in terms of both aerodynamic and aeroacoustic performance.

As a result, two new optimal designs with low noise level and adequate aerodynamic performance were obtained. The overall good agreement of numerical and experimental results indicates the reliability and effectiveness of the present simulation-based

optimization methodology. It can be stated that this method is able to reach optimization objectives efficiently and hence can be used for centrifugal type turbomachinery in order to achieve better performance.

APPENDIX A

Table A.1. DOE matrix

#	inner tip diameter (mm)	inner tip diameter/inner hub diameter	outer diameter(mm)	blade exit angle(°)	blade length(mm)	blade number
1	$D_{1,tip}$-10	1.17	D_2-11	β_2-20	b-6	z
2	$D_{1,tip}$-10	1.17	D_2-22	β_2-10	b-3	z+2
3	$D_{1,tip}$	1.07	D_2-22	β_2-10	b	z
4	$D_{1,tip}$	1.17	D_2-11	β_2-10	b-3	z
5	$D_{1,tip}$	1.17	D_2	β_2	b-3	z-2
6	$D_{1,tip}$	1.27	D_2-22	β_2-10	b-6	z
7	$D_{1,tip}$	1.27	D_2-22	β_2-10	b	z
8	$D_{1,tip}$+10	1.07	D_2-11	β_2	b-3	z
9	$D_{1,tip}$+10	1.17	D_2	β_2-10	b-3	z+2
10	$D_{1,tip}$	1.07	D_2-11	β_2-10	b-6	z-2
11	$D_{1,tip}$+10	1.27	D_2-11	β_2-20	b-3	z
12	$D_{1,tip}$+10	1.17	D_2-11	β_2-20	b-6	z
13	$D_{1,tip}$-10	1.27	D_2-11	β_2-20	b-3	z
14	$D_{1,tip}$	1.27	D_2	β_2-10	b	z
15	$D_{1,tip}$	1.27	D_2-11	β_2-10	b	z-2
16	$D_{1,tip}$-10	1.17	D_2	β_2-10	b-3	z+2
17	$D_{1,tip}$	1.07	D_2-11	β_2-10	b	z-2
18	$D_{1,tip}$+10	1.07	D_2-11	β_2-20	b-3	z
19	$D_{1,tip}$	1.17	D_2-22	β_2	b-3	z+2
20	$D_{1,tip}$	1.17	D_2-11	β_2-10	b-3	z
21	$D_{1,tip}$	1.07	D_2-22	β_2-10	b-6	z
22	$D_{1,tip}$	1.17	D_2-22	β_2-20	b-3	z-2
23	$D_{1,tip}$-10	1.17	D_2-11	β_2	b	z
24	$D_{1,tip}$-10	1.17	D_2-11	β_2-20	b	z
25	$D_{1,tip}$+10	1.17	D_2-11	β_2	b-6	z
26	$D_{1,tip}$	1.17	D_2	β_2-20	b-3	z-2
27	$D_{1,tip}$	1.07	D_2-11	β_2-10	b	z+2
28	$D_{1,tip}$-10	1.27	D_2-11	β_2	b-3	z

29	D_1,tip	1.17	D_2	β_2-20	b-3	z+2
30	D_1,tip-10	1.17	D_2	β_2-10	b-3	z-2
31	D_1,tip	1.27	D_2-11	β_2-10	b-6	z+2
32	D_1,tip	1.17	D_2	β_2	b-3	z+2
33	D_1,tip	1.27	D_2-11	β_2-10	b-6	z-2
34	D_1,tip	1.07	D_2-11	β_2-10	b-6	z+2
35	D_1,tip-10	1.17	D_2-22	β_2-10	b-3	z-2
36	D_1,tip	1.17	D_2-11	β_2-10	b-3	z
37	D_1,tip+10	1.17	D_2-11	β_2-20	b	z
38	D_1,tip-10	1.17	D_2-11	β_2	b-6	z
39	D_1,tip+10	1.27	D_2-11	β_2	b-3	z
40	D_1,tip	1.27	D_2-11	β_2-10	b	z+2
41	D_1,tip+10	1.17	D_2-11	β_2	b	z
42	D_1,tip	1.17	D_2-22	β_2-20	b-3	z+2
43	D_1,tip+10	1.17	D_2-22	β_2-10	b-3	z-2
44	D_1,tip	1.07	D_2	β_2-10	b-6	z
45	D_1,tip	1.17	D_2-22	β_2	b-3	z-2
46	D_1,tip	1.17	D_2-11	β_2-10	b-3	z
47	D_1,tip	1.17	D_2-11	β_2-10	b-3	z
48	D_1,tip-10	1.07	D_2-11	β_2	b-3	z
49	D_1,tip	1.07	D_2	β_2-10	b	z
50	D_1,tip	1.27	D_2	β_2-10	b-6	z
51	D_1,tip-10	1.07	D_2-11	β_2-20	b-3	z
52	D_1,tip+10	1.17	D_2-22	β_2-10	b-3	z+2
53	D_1,tip+10	1.17	D_2	β_2-10	b-3	z-2
54	D_1,tip	1.17	D_2-11	β_2-10	b-3	z

Table A.2. CFD results

#	mass flow rate (kg/s)	vorticity (casing) (1/s)	st_dev pressure (casing) (Pa)
1	0.00909	5.7	1028.6
2	0.01031	6.0	1100.8
3	0.01136	6.7	1219.8
4	0.01085	6.7	1174.7
5	0.01166	7.6	1259.2
6	0.00796	4.9	920.3
7	0.01188	7.2	1244.7
8	0.01016	6.3	1136.7
9	0.01186	7.9	1271.5
10	0.00837	5.2	986.4
11	0.01025	6.1	1126.7
12	0.00824	5.1	970.6
13	0.01111	6.8	1183.2
14	0.01453	10.5	1492.5
15	0.01257	8.0	1324.2
16	0.01285	8.9	1339.9
17	0.01210	7.5	1295.5
18	0.00974	5.7	1095.3
19	0.01013	6.1	1094.1
20	0.01085	6.7	1174.7
21	0.00766	4.7	900.2
22	0.00890	4.8	1007.0
23	0.01360	9.3	1401.1
24	0.01329	8.3	1372.7
25	0.00882	5.9	1024.1
26	0.01130	7.2	1236.1
27	0.01321	8.8	1372.8
28	0.01153	7.5	1226.8
29	0.01212	8.0	1285.9
30	0.01184	7.7	1271.7
31	0.00931	6.2	1048.9
32	0.01273	9.0	1336.1

33	0.00863	5.3	1001.3
34	0.00911	6.0	1033.0
35	0.00956	5.3	1051.3
36	0.01085	6.7	1174.7
37	0.01230	7.7	1304.2
38	0.00967	6.5	1080.0
39	0.01070	6.7	1171.0
40	0.01362	9.2	1395.3
41	0.01242	8.0	1324.4
42	0.00971	5.4	1054.4
43	0.00851	4.7	988.6
44	0.01007	6.9	1142.4
45	0.00930	5.2	1045.9
46	0.01085	6.7	1174.7
47	0.01085	6.7	1174.7
48	0.01130	7.3	1210.2
49	0.01412	10.0	1464.6
50	0.01027	7.0	1149.9
51	0.01087	6.6	1168.9
52	0.00927	5.3	1034.9
53	0.01093	7.0	1210.5
54	0.01085	6.7	1174.7

Table A.3. Correlation matrix

Parameter	mass flow rate (kg/s)	vorticity (casing) (1/s)	st_dev pressure (casing) (Pa)
inner tip diameter (mm)	-0.200	-0.207	-0.156
inner tip diameter/inner hub diameter	0.073	0.076	0.052
outer diameter (mm)	0.503	0.635	0.561
blade exit angle (°)	0.086	0.154	0.096
blade length (mm)	0.809	0.653	0.788
blade number	0.179	0.226	0.138

Table A.4. Comparison of baseline and optimal design (2-D optimization)

#	impeller vorticity (1/s)	casing vorticity (1/s)	ΔP (Pa)	point_fft_1	point_fft_2
Baseline	579.6	127.2	42124.2	409363.2	79187.4
Optimal	493.7	94.4	39891.4	287252.6	57353.1

Figure A.1. Prototype of Pareto 1

Figure A.2. Prototype of Pareto 2

REFERENCES

1. Grapsas, A., J. S. Anagnostopoulos and E. Papantonis, *"Parametric Study and Design Optimization of a Radial Flow Pump Impeller"*, 2nd International Conference "From Scientific Computing to Computational Engineering", Athens, 5-8 July, 2006.

2. Burguburu, S. and A. Pape, *"Improved Aerodynamic Design of Turbomachinery Bladings by Numerical Optimization"*, Aerospace Science and Technology, vol. 7, pp 277-287, 2003.

3. Mengistu, T. and W. Ghaly, *"Aerodynamic Optimization of Turbomachinery Blades Using Evolutionary Methods and ANN-based Surrogate Models"*, Optim. Eng., vol.9, pp. 239-255, 2008.

4. Pierret, S., *"Multi-objective and Multi-Disciplinary Optimization of Three-dimensional Turbomachinery Blades"*, 6th World Congress of Structural and Multidisciplinary Optimization, Brazil, 2005.

5. Kelner, V., G. Grondin and O. Leonard, *"Multi-objective Optimization of a Fan Blade by Coupling a Genetic Algorithm and a Parametric Flow Solver"*, EUROGEN, Munich, 2005.

6. Han, S. Y. and J. S. Maeng, *"Shape Optimization of Cut-off in a Multi-blade Fan/Scroll System Using Neural Network"*, International Journal of Heat and Mass Transfer, pp. 2833-2839, 2003.

7. Sun, H., H. Shin and S. Lee, *"Analysis and Optimization of Aerodynamic noise in a Centrifugal Compressor"*, Journal of Sound and Vibration, vol. 289, pp. 999-1018, 2005.

8. Tu, J., G. H. Yeoh and C. Liu, *"Computational Fluid Dynamics"*, Butterworth-Heinemann, 2008.

9. Gülich, J., "*Centrifugal Pumps*", Springer, 2008.

10. Nilsson, H., "*Assessment of Turbulence Modelling for CFD Simulations into Hydroturbines: Spiral Casings*", 17th International Mechanical Engineering Congress, 2003.

11. Wilcox, D. C., "*Re-assessment of the scale-determining Equation for Advanced Turbulence Models*", AIAA Journal, vol. 26, pp. 1414-1421, 1988.

12. Tsai, C. H., L. M. Fu, Tai, Y. L. Huang and Leong, "*Computational Aero-acoustic Analysis of a Passenger Car with a Rear Spoiler*", Applied Mathematical Modelling, vol. 33, pp. 3661-3673, 2009.

13. Cengel, Y. and J. Cimbala, "*Fluid Mechanics: Fundamentals and Applications*", McGraw-Hill, 2007.

14. Hauser, J. and Y. Xia, "*Modern Introduction to Grid Generation*", COSMASE Short Course Notes, Lausanne, 1996.

15. Lighthill, M. J., "*On Sound Generated Aerodynamically I. General Theory*", Proceedings of the Royal Society of London, vol. 211, pp. 564-587, 1952.

16. Curle, N., "*The Influence of Solid Boundaries upon Aerodynamic Sound*", Proceedings of the Royal Society of London, vol. 231, pp. 505-514, 1955.

17. Ffowcs Williams, J. E. and D. L. Hawkings, "*Sound Generation by Turbulence and Surfaces in Arbitrary Motion*", Philosophical Transactions of the Royal Society of London, vol. 264, pp. 321-342, 1969.

18. Moore, P. and B. Boersma, "*Use of Surface Integral Methods in the Computation of the Acoustic Far field of a Turbulent Jet*", Springer Netherlands, 2006.

19. Khelladi, S., S. Kouidri, F. Bakir and R. Rey, "*Predicting Tonal Noise from a High Rotational Speed Centrifugal Fan*", Journal of Sound and Vibration, vol. 313, pp. 113-133, 2007.

20. Howe, M. S., "*Theory of a Vortex Sound*", Cambridge University Press, 2002.

21. Jang, C. M. and K. Y. Kim, "*Optimization of a Stator Blade Using response Surface Method in a Single-Stage Transonic Axial Compressor*", Journal of Power and Energy, vol. 219, pp. 595-603, 2005.

22. Behzadmehr, A., Y. Mercadier and N. Galanis, "*Sensitivity Analysis of Entrance Design Parameters of Backward-Inclined Centrifugal Fan Using Doe Method and CFD Calculations*", Journal of Fluids Eng., vol. 128, 2006.

23. Anderson, M. and P. Whitcomb, "*RSM simplified: Optimization Processes Using response Surface Methods for Design of Experiments*", Productivity Press, 2005.

24. Kantas, M., "*Ev Tipi Elektrikli Fırınların Performansının Sayısal ve Deneysel İncelenmesi*", Yıldız Technical University, 2007.